



ELSEVIER

Physica D 162 (2002) 155–187

PHYSICA D

www.elsevier.com/locate/physd

Heteroclinic dynamics in the nonlocal parametrically driven nonlinear Schrödinger equation

M. Higuera^{a,b}, J. Porter^{c,b}, E. Knobloch^{c,d,*}

^a *E.T.S.I. Aeronáuticos, Universidad Politécnica de Madrid, 28040 Madrid, Spain*

^b *Department of Engineering Sciences and Applied Mathematics, Northwestern University, Evanston, IL 60208, USA*

^c *Department of Physics, University of California, Berkeley, CA 94720, USA*

^d *Department of Applied Mathematics, University of Leeds, Leeds LS2 9JT, UK*

Received 7 November 2000; received in revised form 2 July 2001; accepted 1 November 2001

Communicated by A. Doelman

Abstract

Faraday waves are described, under appropriate conditions, by a damped nonlocal parametrically driven nonlinear Schrödinger equation. As the strength of the applied forcing increases this equation undergoes a sequence of transitions to chaotic dynamics. The origin of these transitions is explained using a careful study of a two-mode Galerkin truncation and linked to the presence of heteroclinic connections between the trivial state and spatially periodic standing waves. These connections are associated with cascades of gluing and symmetry-switching bifurcations; such bifurcations are located in the partial differential equations as well. © 2002 Elsevier Science B.V. All rights reserved.

Keywords: Parametric instability; Nonlinear Schrödinger equation; Global bifurcation

1. Introduction

The effect of parametric forcing on continuous systems undergoing a Hopf bifurcation has received considerable attention in the past few years [1–4]. In the absence of forcing, systems with only one extended dimension (hereafter x) and reflection symmetry (i.e. invariance under $x \rightarrow -x$) support both traveling and standing waves, at most one of which can be stable. Parametric forcing is known to stabilize the latter even when these states would otherwise be unstable to traveling wave disturbances [1]. Similar behavior occurs even in the absence of the primary Hopf bifurcation. In this case both wave types decay but the standing waves can be maintained against decay by parametric forcing. The Faraday system [5] provides perhaps the best known example of this setup. In this system standing surface waves with frequency near ω_0 are excited by vertical vibration of a container of liquid with frequency $2\omega_0$. In a narrow annular container the Faraday system becomes essentially one-dimensional, and near threshold of the Faraday instability the physical variables can be written as a superposition of two counterpropagating waves:

$$u(x, t) = [A(x, t)e^{i\omega_0 t + ikx} + B(x, t)e^{i\omega_0 t - ikx} + \text{c.c.}]u_0 + \dots \quad (1)$$

* Corresponding author. Tel.: +1-510-642-3395; fax: +1-510-643-8497.

E-mail address: knobloch@physics.berkeley.edu (E. Knobloch).

Here ω_0 is half the forcing frequency and k is the associated wavenumber. The complex amplitudes, A and B , are assumed to be small and to depend slowly on x and t , i.e. $|A_{xx}| \ll |A_x| \ll |A|$, $|B_{xx}| \ll |B_x| \ll |B|$, $|A_t| \ll |A|$ and $|B_t| \ll |B|$. When the dissipation is appropriately weak and the amplitude of the forcing correspondingly small the amplitudes A and B satisfy a pair of evolution equations that are coupled to a two-dimensional Navier–Stokes equation for a large-scale mean flow in the bulk [6]. This mean flow is driven by boundary conditions obtained by matching the solutions in the oscillatory boundary layers near the bottom and the free surface to the bulk flow. While complicated such equations already provide a simplified description of the Faraday system since the fast oscillation frequency has been eliminated and the boundary conditions on the mean flow are imposed on the undisturbed surface. Moreover, in particular regimes a further simplification is possible, as discussed in [6]. These depend on the relative magnitude of the detuning ν , damping δ , and forcing amplitude μ , and the inverse aspect ratio L^{-1} of the domain. When L is large compared to the wavelength of the excited waves, and $\nu \sim \delta \sim \mu \sim L^{-1}$ the growth of the instability occurs on the timescale corresponding to advection at the group velocity c_g (hereafter scaled such that $c_g = 1$), while the dispersive terms are of higher order, i.e. $O(L^{-2})$. The slow evolution of the system is then described by a *hyperbolic* system of partial differential equations for A and B . In contrast, in the regime of interest here, $\nu \sim \delta \sim \mu \sim L^{-2}$, advection at the group velocity is *fast* compared to the growth rate of the instability, and the evolution equations are then written in terms of the characteristic variables $\eta = (t + x)/L$ and $\xi = (t - x)/L$. These take the form of a pair of damped parametrically driven nonlinear Schrödinger (NLS) equations with nonlocal coupling [6,7],

$$A_\tau = i\alpha A_{\eta\eta} - (\delta + i\nu)A + i(\beta|A|^2 + \gamma\langle|B|^2\rangle)A + \mu\langle\bar{B}\rangle, \quad (2)$$

$$B_\tau = i\alpha B_{\xi\xi} - (\delta + i\nu)B + i(\beta|B|^2 + \gamma\langle|A|^2\rangle)B + \mu\langle\bar{A}\rangle, \quad (3)$$

together with a decoupled equation that relates the spatial phase of the waves to the mean flow they generate whenever $|A| \neq |B|$. Eqs. (2) and (3) are to be solved subject to the boundary conditions

$$A(\eta + 1, \tau) = A(\eta, \tau), \quad B(\xi + 1, \tau) = B(\xi, \tau) \quad (4)$$

appropriate for a periodic (i.e. annular) domain of length L . Here $\langle \dots \rangle \equiv \int_0^1 \dots d\eta$ or $\int_0^1 \dots d\xi$, $\tau \equiv t/L^2$, and $\alpha, \delta, \nu, \beta, \gamma, \mu \in \mathbb{R}$, with α, β , and γ measuring the magnitude of the dispersion, self-interaction, and cross-interaction terms, respectively.

The form of these equations relies on the presence of three timescales: a fast $O(1)$ timescale determined by the frequency of the applied forcing, a slow $O(L^{-1})$ advective timescale determined by the group velocity and the domain size L , and an even slower $O(L^{-2})$ timescale over which the instability develops and equilibrates. The nonlocal terms, $\langle \dots \rangle$, arise because under the current scaling assumptions the timescale on which the spatial inhomogeneities are advected is fast relative to the slower timescale on which damping, dispersion, and nonlinear terms act. This timescale separation is the reason why the wavetrains interact only via the average of their amplitudes over the advective timescale. In generic systems the large-scale flow is damped rapidly, and the resulting equations are those derived by Knobloch and De Luca [8]. In the present case, the assumed weak dissipation is responsible for two additional features of the problem, the coupling of the spatial phase to the weakly damped large-scale mean flow, and the presence of purely imaginary coefficients of the dispersive and nonlinear terms. Real parts of these coefficients enter only at higher order in the theory. This is so also in nonlinear optics, where related equations describe the propagation of electromagnetic waves along an optical fiber in a ring geometry [9] and, under certain conditions, explain the subcritical bistable behavior of both front and pulse solutions in degenerate optical parametric oscillators [10]. In these systems coupling to a large scale mode does not arise.

Observe that Eqs. (2)–(4) have an invariant subspace $A(\cdot, \tau) = B(\cdot, \tau)$ ($=C(\cdot, \tau)$, say), in which the dynamics are described by the following equations:

$$C_\tau = i\alpha C_{xx} - (\delta + i\nu)C + i(\beta|C|^2 + \gamma\langle|C|^2\rangle)C + \mu\langle\bar{C}\rangle, \quad (5)$$

$$C(x+1, \tau) = C(x, \tau). \quad (6)$$

Hereafter the variable x stands for either η or ξ , depending on whether C stands for A or B . Eqs. (5) and (6) describe *standing wave* (hereafter SW) solutions of Eqs. (2)–(4); such solutions are a characteristic property of systems that are invariant under spatial reflection $x \rightarrow -x$, and do not generate a mean flow. Martel et al. [7] show that identical equations also describe standing waves in a system bounded by lateral walls, provided only that the reflection coefficient at the walls is close to unity, i.e. provided the walls are almost perfectly reflecting. Although this paper is devoted to the study of the simpler system defined by Eqs. (5) and (6) it must be emphasized that at large enough forcing amplitude the SW may become unstable to perturbations transverse to the SW subspace; if this is so the dynamics of Eqs. (2)–(4) and Eqs. (5)–(6) will differ (see Fig. 1). Such instabilities are associated with the spontaneous generation of mean flows [11].

The dynamics of the systems (2)–(4) and (5)–(6) have been studied by Martel et al. [7]. In the following we refer to solutions that are independent of τ as steady; such solutions describe single frequency waves, oscillating at the frequency ω . In both (2)–(4) and (5)–(6) the first instability produces uniform steady solutions (corresponding to periodic standing waves in both space and time) and these subsequently lose stability in a steady-state symmetry-breaking bifurcation that breaks translation invariance producing time-independent but spatially nonuniform states (i.e. standing waves with spatially varying amplitude). Both these bifurcations preserve the identity $A = B$ and hence are common to both sets of equations. As shown by Martel et al. [7] the subsequent behavior of these equations can be divided into four broad classes, depending on the linear stability properties of the spatially uniform steady solutions. These classes are therefore the same for both sets of equations. In the case shown in Fig. 1a and b the nonuniform states soon undergo a Hopf bifurcation and produce a branch of oscillatory solutions. Shortly thereafter chaos sets in, interspersed with nonuniform temporally periodic motion. Some of the observed transitions are the result of crises while others appear to be due to period-doubling cascades. Observe that the details of this behavior differ in the two figures, indicating that the invariant subspace $A = B$ does not remain attracting for all values of μ . The present paper is devoted to understanding of the origin of this more complicated dynamical behavior in the simpler of these two systems, viz. (5)–(6).

Analysis of the system (5)–(6) is complicated by the absence of wavenumber-dependent dissipation: the damping (measured by the coefficient δ) is *identical* for all modes. Although such damping implies the absence of wavenumber selection through dissipative processes in the present problem this fact poses no problem since the wavenumber is selected by the forcing frequency via the dispersion relation for gravity–capillary waves. However, the absence of dissipation at leading order does result in a number of mathematical difficulties. For example, the theorem of Duan et al. [12] establishing the existence of a finite-dimensional inertial manifold for a nonlocal Ginzburg–Landau equation of the type (5)–(6) does not apply. Nonetheless, for the weakly damped NLS equation with direct external forcing, Ghidaglia [13] was able to demonstrate the existence of a weak finite-dimensional attractor. This result was improved upon by Wang [14] who used an energy equation to obtain strong convergence, showing that the attractor is in fact a strong, finite-dimensional, global attractor. Subsequent work (see, e.g. [15,16]) has dealt with the task of proving additional regularity properties of the attractor. In particular, Oliver and Titi [16] showed that the global attractor for the weakly damped driven (but local) NLS equation with direct forcing is analytic, indicating that the Fourier expansion of a solution on the attractor converges exponentially fast (as the number of terms is increased) to the exact solution. We assume here that these properties continue to hold for the nonlocal equation with parametric forcing, and construct a simple truncation of Eqs. (5) and (6) involving two complex mode amplitudes. We find that

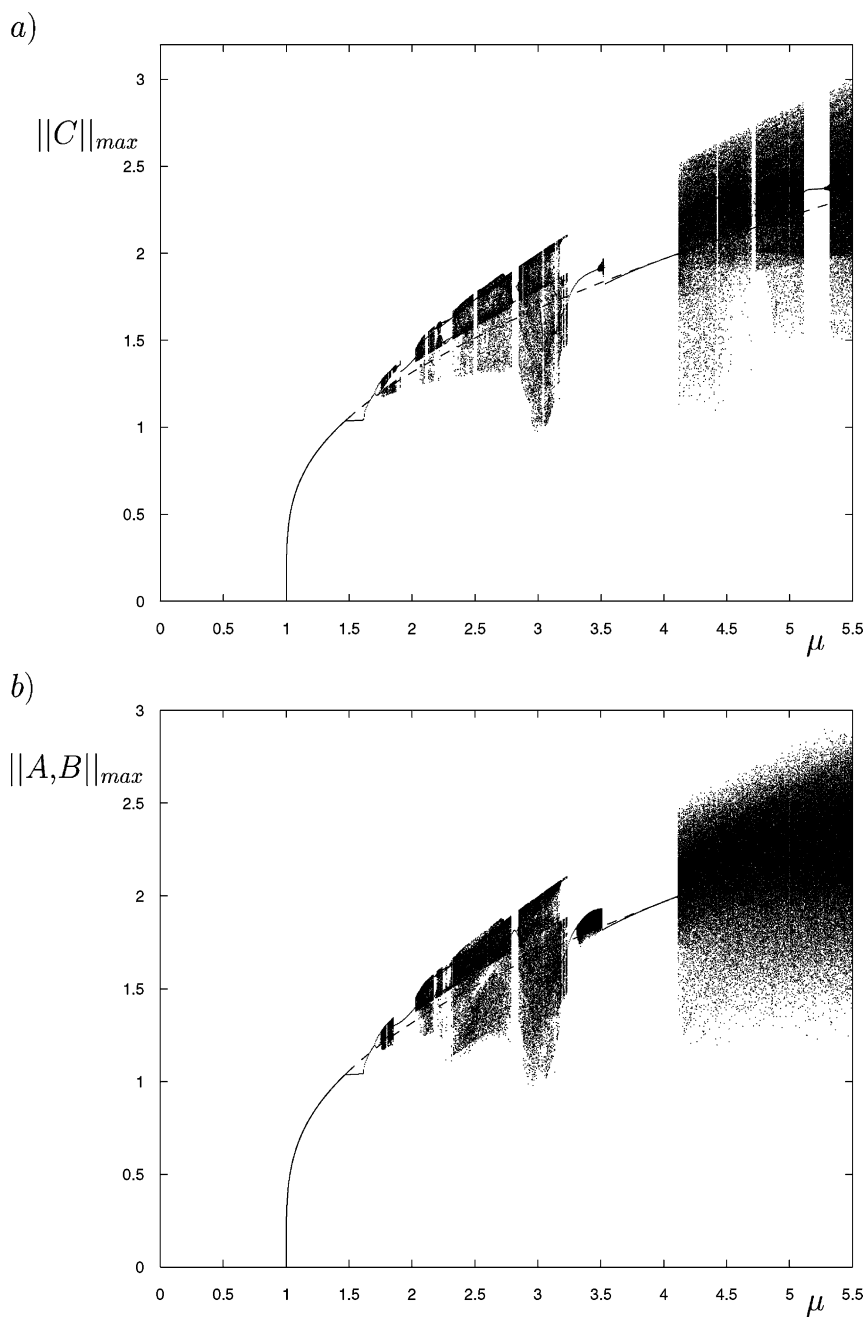


Fig. 1. Bifurcation diagrams for (a) the system (5)–(6), and (b) the system (2)–(4) with $\alpha = 0.1$, $\delta = 1$, $\nu = 0$, $\beta = 1.5$, and $\gamma = -0.5$. Courtesy C. Martel.

in relatively large regions of parameter space this truncation describes the observed dynamics very well, and use it to elucidate their origin and to locate additional solution types in the partial differential equations (PDEs) that were missed by Martel et al.

The analysis of low-order models of PDEs is a commonly used technique which often provides considerable insight into the dynamics of the PDEs. This technique was particularly successful in studies of doubly diffusive systems (see [17] for a review), and more recently has been used with similar success to understand the behavior of both the complex Ginzburg–Landau equation [18–20], and the dynamics in the weakly damped driven sine-Gordon equation [21,22]. This last example is closest to the spirit of the present paper. After time-averaging, this system can be written in the form of an autonomous weakly damped NLS equation with direct forcing. When the forcing is appropriately small a two-mode description of this system can be written as a perturbed two-degree-of-freedom completely integrable Hamiltonian system. Wiggins and co-workers [22–25] developed a general geometric theory for systems of this type that describes the changes that occur under both Hamiltonian and non-Hamiltonian perturbations, including the generation of multipulse orbits, and their progressive destruction as the damping increases. Since the underlying Hamiltonian system for the problem under investigation is identical to that studied by these authors, we expect that much of this behavior carries over to the non-Hamiltonian perturbation encountered in our problem, provided only that it is sufficiently small. In our case, however, the presence of the symmetry $C \rightarrow -C$ and the concomitant trivial state $C = 0$ exert a profound effect on the behavior of the system. As a result in our system much interesting dynamics occur ‘far’ from the Hamiltonian limit that would not be expected of the corresponding system with direct forcing. It is this regime that is the subject of the present paper. By near-Hamiltonian we mean that $\delta, \mu \ll O(L^{-2})$ while the term far-from-Hamiltonian refers to $\delta, \mu = O(L^{-2})$. As shown below in the latter regime the system (5)–(6) exhibits dynamics that resemble more closely those familiar from studies of D_2 -symmetric dynamical systems, such as the shearing instability of convection or magnetoconvection [26,27], rather than the damped nonlinear Schrödinger equation with direct forcing. We begin Section 2 by discussing the symmetries of Eqs. (5) and (6), and summarizing the properties of their simplest solutions. We then introduce the two-mode truncation of these equations and describe in Section 3 the results of a detailed numerical study of this two-mode model. Much of the behavior is seen to be organized by a heteroclinic bifurcation involving the trivial and the nontrivial but spatially uniform states. This bifurcation is associated with infinite cascades of gluing and symmetry-switching bifurcations which themselves give rise to chaotic dynamics of Shil’nikov type. In Section 4 we construct analytically Poincaré maps to investigate the properties of this heteroclinic bifurcation and to understand the role of the symmetries of the PDEs in generating the dynamics that accompany it. In Section 5 the two-mode model is used to locate solutions in the PDEs resembling the results from the ordinary differential equations (ODEs) at identical parameter values, and its limitations for understanding the PDE results are examined. Implications of our work for the Faraday problem are discussed in the concluding section.

2. The two-mode model

In this section we introduce the two-mode truncation of Eqs. (5) and (6) which we write in the simpler form

$$C_\tau = -(1 + i\nu)C + i\alpha C_{xx} + i[|C|^2 + (\Lambda - 1)\langle |C|^2 \rangle]C + \mu \langle \bar{C} \rangle, \quad (7)$$

$$C(x + 1, \tau) = C(x, \tau), \quad (8)$$

using the rescaling

$$\tau \rightarrow \frac{\tau}{\delta}, \quad C \rightarrow \sqrt{\frac{\delta}{|\beta|C}}, \quad (\alpha, \nu, \mu) \rightarrow \delta(\alpha, \nu, \mu). \quad (9)$$

If $\beta < 0$ the transformation $(C, \alpha, \nu) \rightarrow (\bar{C}, -\alpha, -\nu)$ is performed first. Here the relative size of the nonlinear terms is measured by the single real parameter $\Lambda \equiv 1 + \gamma/\beta$. In view of the above scaling all of the coefficients appearing in Eq. (7) are formally $O(1)$. Due to the periodic boundary conditions $C(x, \tau)$ may be expanded in a Fourier series,

$$C(x, \tau) = \sum_{n=-\infty}^{\infty} C_n(\tau) e^{i2\pi n x}, \quad (10)$$

which, upon substitution into Eq. (7), yields an infinite set of ODEs:

$$\dot{C}_n = -(1 + i\nu_n)C_n + \mu\delta_{n0}\bar{C}_0 + i(\Lambda - 1)C_n \sum_{k=-\infty}^{\infty} |C_k|^2 + \sum_{k-l+m=n} C_k \bar{C}_l C_m. \quad (11)$$

Here the dot denotes differentiation with respect to τ , δ_{n0} is the Kronecker delta, $\nu_n \equiv \nu + \alpha(2\pi n)^2$, and the last summation is a triple sum over integers k, l , and m with each variable ranging from $-\infty$ to ∞ . Observe that due to the spatial (i.e. x -) averaging, the forcing only couples to the *uniform* mode, C_0 . Consequently, the trivial state is always stable with respect to nonuniform modes ($n > 0$) and the only primary bifurcation is to the nontrivial uniform state ($C_0 \neq 0, C_n = 0$ if $n \neq 0$).

Eqs. (7) and (8) are equivariant under the actions of the following three symmetries:

$$T_\chi : x \rightarrow x + \chi, \quad \mathcal{R} : x \rightarrow -x, \quad \hat{k} : C \rightarrow -C, \quad (12)$$

which generate the group $\Gamma \equiv O(2) \times \mathbb{Z}_2$. The first two symmetries together generate the group $O(2)$, while the last symmetry, $\hat{k} \in \mathbb{Z}_2$, is a manifestation of the invariance of the original problem under translations through a half period on the fast temporal scale (a full period of the forcing), and is a consequence of the parametric nature of the forcing. These symmetries, when viewed within the expansion (11) are responsible for the existence of multiple invariant subspaces. These include the *uniform subspace* corresponding to spatially uniform solutions ($C_n = 0$ if $n \neq 0$), fixed by $O(2)$; the *even subspace* ($C_n = 0$ if n is odd), fixed by $T_{1/2}$; the *odd subspace* ($C_n = 0$ if n is even), fixed by $\hat{k}T_{1/2}$; the *cosine subspace* ($C_n = C_{-n}$), fixed by \mathcal{R} ; and the *sine subspace* ($C_n = -C_{-n}$), fixed by $\hat{k}\mathcal{R}$. In fact, the action of T_χ on either of the last two subspaces generates an entire circle of equivalent subspaces.

Since the first bifurcation from the trivial solution as μ increases is always a Γ -breaking pitchfork which produces a pair of uniform states (related by \hat{k}) it is the secondary bifurcations which are of greatest interest. To study them we write the uniform states in the form $C_0 = a e^{i\vartheta}$, where

$$\Lambda a^2 = \nu \pm \sqrt{\mu^2 - 1}, \quad \cos 2\vartheta = \frac{1}{\mu}. \quad (13)$$

After linearizing Eqs. (11) about this solution we find that it is unstable to uniform perturbations when $a^2 < \nu/\Lambda$. More precisely, if $\nu\Lambda > 0$ the primary pitchfork is subcritical and the state (13) is unstable to uniform perturbations until a saddle-node bifurcation at $\mu = 1$. Stability with respect to modes with $n > 0$ is described by the dispersion relations

$$(s + 1)^2 + (\nu_n - \Lambda a^2)^2 + 2a^2(\Lambda a^2 - \nu_n) = 0. \quad (14)$$

The corresponding neutral stability curves in the (Λ, a) plane are illustrated in Fig. 2a for $\alpha = 0.1$ and $\nu = 0$. Note that there are three distinct regions. If $\Lambda > 0$ and a (equivalently, μ) is increased the uniform state repeatedly enters and emerges from an infinite series of perhaps overlapping instability tongues. As $\Lambda \rightarrow 0+$ the latter bifurcation occurs at higher and higher amplitude (cf. Eq. (13)) with the amplitude becoming infinite in the limit as $\Lambda \rightarrow 0+$. Within each tongue the uniform mode is unstable with respect to the corresponding mode. If $-2 < \Lambda < 0$ the

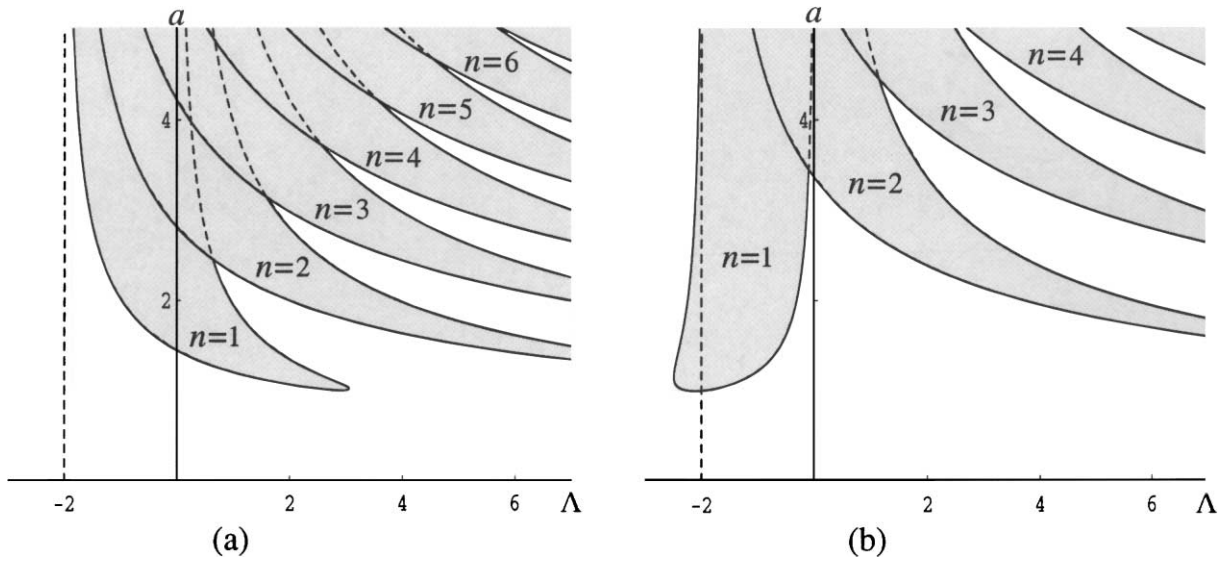


Fig. 2. Neutral stability curves for (a) $\alpha = 0.1$, $\nu = 0$ and (b) $\alpha = 0.2$, $\nu = -9$.

uniform state enters (and does not leave) successively higher and higher instability tongues, accumulating instability as it does so. Lastly, if $\Lambda < -2$ there are no secondary bifurcations and the uniform state remains stable for all μ . For other choices of α and ν this last situation may be modified, as seen in Fig. 2b for $\alpha = 0.2$ and $\nu = -9$. Large detuning has an especially visible effect on the shape of the instability tongues when n is small but is less important for higher modes. Neutral stability curves for $\alpha < 0$ can be obtained from the transformation $(\alpha, \nu, \Lambda) \rightarrow -(\alpha, \nu, \Lambda + 2)$ which leaves Eq. (14) invariant. This transformation, however, changes the amplitude a , and so is not a symmetry of Eq. (7). As a result the properties of Eq. (7) for $\alpha > 0$ and $\alpha < 0$ are quite different (see Fig. 3). Fig. 3b indicates that, for $\alpha = -0.1$ and $-2 < \Lambda < 0$, the uniform state loses stability to each mode just once as μ increases, with the amplitude at which it does so tending to infinity both with the mode number and as $\Lambda \rightarrow 0^-$ (cf. Eq. (13)).

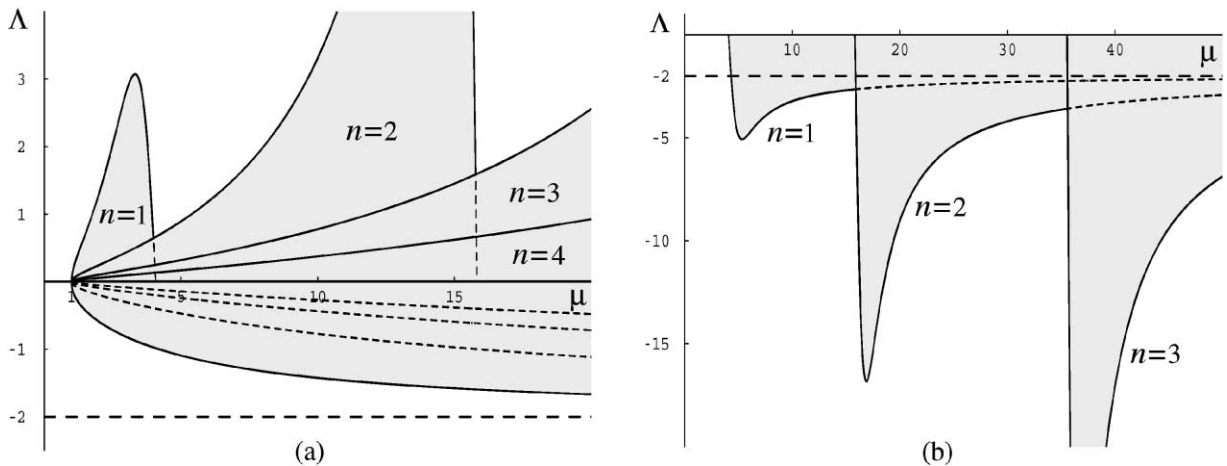


Fig. 3. Neutral stability curves for $\nu = 0$: (a) $\alpha = 0.1$; (b) $\alpha = -0.1$. In (a) only four curves are shown but all curves ($n \geq 1$) pass through $(\mu, \Lambda) = (1, 0)$.

When $\Lambda = 0$ the system (7)–(8) is highly degenerate, as can be seen by examining the subspace of spatially uniform solutions:

$$\dot{C}_0 = -(1 + i\nu)C_0 + \mu\bar{C}_0. \quad (15)$$

Due to the complete cancellation of the nonlinear terms for $\Lambda = 0$ the flow in this subspace is linear and, when $\mu^2 > 1 + \nu^2$, unbounded. The branch of uniform states (plotted versus μ) is completely vertical; a *line* of such states exists when $\mu^2 = 1 + \nu^2$ but for no other values of μ , cf. [28]. Despite this nongeneric behavior, we will see in Section 3 that the limit $\Lambda = 0$ plays a crucial role in understanding the complex behavior exhibited by Eqs. (7) and (8) for nonzero values of Λ .

As already mentioned, we hope to gain insight into the properties of the full system (7)–(8) with the aid of a low-dimensional model. To construct one, we observe that the primary bifurcation in Eqs. (7) and (8) is to a nontrivial uniform state while the secondary bifurcation of this state produces a steady nonuniform state, both of which are symmetric with respect to the reflection \mathcal{R} and hence lie in the invariant cosine subspace (or a translation of it). Consequently, we focus on the class of reflection-invariant solutions to Eqs. (7) and (8), i.e. solutions of the form

$$C(x, \tau) = \frac{1}{\sqrt{2}}c_0(\tau) + \sum_{n=1}^{\infty} c_n(\tau) \cos 2\pi nx, \quad (16)$$

and retain only the first two terms:

$$C(x, \tau) = \frac{1}{\sqrt{2}}c_0(\tau) + c_1(\tau) \cos 2\pi x. \quad (17)$$

Note the factor of $\sqrt{2}$ relating c_0 to C_0 . A similar procedure has been employed with success for the Kuramoto–Sivashinsky [29] and complex Ginzburg–Landau equations [19,20]. Substituting the ansatz (17) into Eq. (7) yields the following two-mode ODE model:

$$\dot{c}_0 = -(1 + i\nu)c_0 + \frac{1}{2}i\Lambda(|c_0|^2 + |c_1|^2)c_0 + \frac{1}{2}i(\bar{c}_0c_1 + \bar{c}_1c_0)c_1 + \mu\bar{c}_0, \quad (18)$$

$$\dot{c}_1 = -(1 + i\nu_1)c_1 + \frac{1}{2}i\Lambda(|c_0|^2 + |c_1|^2)c_1 + \frac{1}{2}i(\bar{c}_0c_1 + \bar{c}_1c_0)c_0 + \frac{1}{4}i|c_1|^2c_1. \quad (19)$$

These equations, for which the action of \mathcal{R} is now trivial, are still equivariant under the actions of $T_{1/2}$ and \hat{k} but we choose instead to define the equivalent pair of operations:

$$R_0 : (c_0, c_1) \rightarrow (-c_0, c_1), \quad R_1 : (c_0, c_1) \rightarrow (c_0, -c_1), \quad (20)$$

where $R_0 = \hat{k}T_{1/2}$ and $R_1 = T_{1/2}$. These actions generate the group D_2 (as did $T_{1/2}$ and \hat{k}). As a result the equations share many features common to other systems with D_2 symmetry [26,27].

Eqs. (18) and (19) contain three types of fixed points whose properties are summarized below. In what follows we write $c_0 \equiv x_0 + iy_0$, $c_1 \equiv x_1 + iy_1$, where x_0, x_1, y_0 and y_1 are all real, and set $\nu = 0$. In general the presence of detuning is a consequence of a slight mismatch between the wavenumber selected by the forcing frequency 2ω and the domain length L . However, the passage through the different resonance tongues identified in the linear theory of [7] does not depend on the exact value of ν adopted despite the fact that the initial pitchfork bifurcation to spatially uniform states U becomes subcritical if $\nu\Lambda < 0$. Moreover, under appropriate nondegeneracy conditions for the eigenvalues involved, the global connections discussed in Sections 3 and 4 persist under the addition of (small) detuning. Thus, the choice $\nu = 0$ is made merely for simplicity and ease of comparison with [7].

2.1. Trivial state (O)

This solution has the full symmetry D_2 . Its stability is determined by the four eigenvalues $\pm\mu - 1$ and $-1 \pm i\omega$, where $\omega \equiv 4\pi^2\alpha$. The first two give the growth rate of perturbations within the invariant plane $c_1 = 0$, while the complex conjugate pair describes perturbations within the invariant plane $c_0 = 0$. When $\mu = 1$ there is a supercritical pitchfork bifurcation giving rise to a branch of spatially uniform states U: $c_0 \neq 0$, $c_1 = 0$; note that there are no fixed points of the form $c_0 = 0$, $c_1 \neq 0$.

2.2. Uniform steady states (U)

These solutions take the form $c_0 \neq 0$, $c_1 = 0$, and are invariant under R_1 but not under R_0 ; when necessary we distinguish between the two R_0 -related branches using the notation U_{\pm} (the \pm reflects the sign of the x_0 coordinate). From Eq. (13) we obtain

$$|\Lambda| |c_0|^2 = 2\sqrt{\mu^2 - 1}, \quad \cos 2\vartheta = \frac{1}{\mu}, \quad (21)$$

where ϑ is again the phase of c_0 . Since $\nu = 0$ (see above) these solutions are always stable to perturbations within the plane $c_1 = 0$ with the corresponding eigenvalues, s , satisfying

$$(s + 1)^2 - (5 - 4\mu^2) = 0. \quad (22)$$

Note that these eigenvalues are complex when $\mu > \sqrt{5}/2$. Stability with respect to the mode c_1 is described by the characteristic equation (cf. Eq. (14))

$$(s + 1)^2 + \omega^2 + \mu^2 - 1 + \frac{2}{\Lambda}(\mu^2 - 1) - \frac{2\omega}{|\Lambda|}(\Lambda + 1)\sqrt{\mu^2 - 1} = 0, \quad (23)$$

where again $\omega = 4\pi^2\alpha$. Thus, when $s = 0$, the uniform states U undergo a pitchfork bifurcation which breaks the R_1 symmetry and produces time-independent nonuniform states with $n = 1$ (NU). In the following we refer to this bifurcation as a symmetry-breaking bifurcation (SB) since it produces states that break translation invariance. Note that because of the form of Eqs. (22) and (23) Hopf bifurcations are not possible.

2.3. Nonuniform steady states (NU)

The fixed points NU have no symmetry; consequently, the NU solutions come in quartets, related by the actions of R_0 , R_1 , and R_0R_1 . Depending on the value of Λ , the NU states may become unstable, with increasing μ , at either a saddle-node or a Hopf bifurcation. If a Hopf bifurcation occurs it generates four symmetry-related periodic orbits. The fate of these and other time-dependent solutions is investigated in the following section.

Since Eqs. (18) and (19) are exact in the invariant uniform subspace of the PDE we may expect them to be quantitatively correct only near the threshold predicted by Eq. (23), i.e. near the stability threshold for the $n = 1$ mode shown in Fig. 3. In fact, as discussed in detail in Section 5, their qualitative validity extends much beyond this region. Consequently, we focus in the next section on the properties of these equations for general values of the parameter μ .

3. Numerical results

In this section we present the results of a careful numerical investigation of Eqs. (18) and (19) using a combination of AUTO [30] and XPPAUT [31]. In addition to the simple bifurcations mentioned above these equations can exhibit

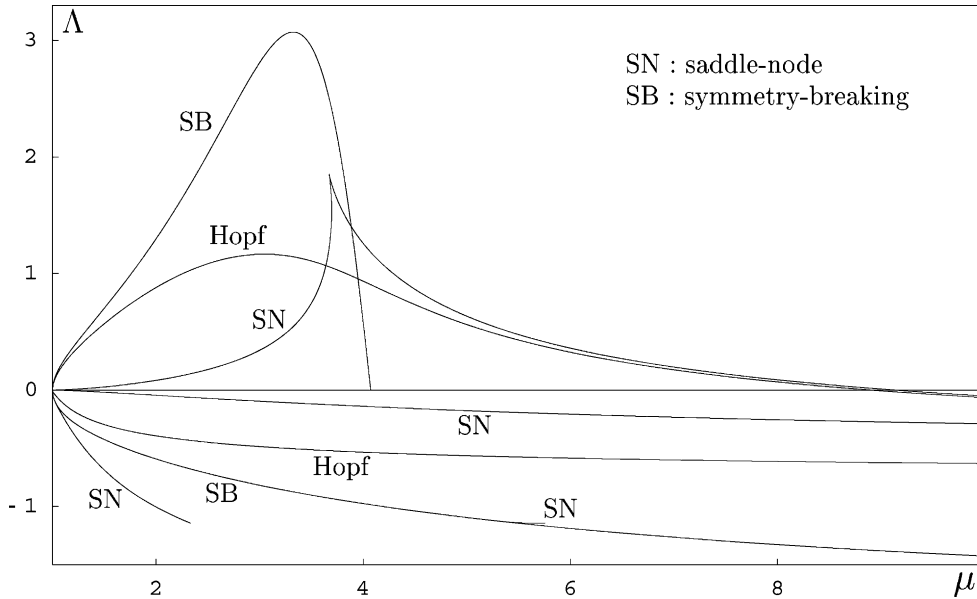


Fig. 4. Local bifurcation sets with $\nu = 0$ and $\alpha = 0.1$: symmetry-breaking bifurcation (SB) on the U branch, and Hopf and saddle-node (SN) bifurcations on the NU branch.

extremely complicated dynamics. We find that over a large range of parameters this complex behavior is organized by a codimension-one heteroclinic connection between the uniform and trivial states, a global bifurcation which can be best understood in the context of a two-parameter study. We therefore set $\nu = 0$, $\alpha = 0.1$ and vary Λ along with the forcing amplitude μ .

Fig. 4 shows the important local bifurcation sets in the (μ, Λ) plane: the $n = 1$ neutral stability curve (labeled SB) from Fig. 3a and the loci of Hopf and saddle-node (SN) bifurcations on the NU branch which bifurcates from the U state along the neutral curve. Fig. 5 shows the bifurcation diagrams obtained on traversing this plane in the direction of increasing μ at several different (but fixed) values of Λ . Fig. 4 reveals the presence of two singularities. There is, as discussed in Section 2, a degeneracy when $\Lambda = 0$; at this value of Λ spatially uniform states exist only at $\mu = 1$ and at no other value of μ . It is thus not surprising that there are many bifurcation sets emanating from the singular point $(\mu, \Lambda) = (1, 0)$. The same type of singular behavior was observed in a model of the shearing instability [27] in the limit of vanishing Prandtl number. In the present problem there is, in addition, evidence of singular behavior at $\Lambda \simeq -1.1428$, where the amplitude of the NU branch (but not the U branch) becomes infinite. As Λ decreases toward this value the two saddle-node bifurcations on the NU branch (at $\mu \sim 2.33$ and 5.67) occur at roughly constant μ values but at larger and larger amplitude (see Fig. 5g). When $\Lambda < -1.1428$ these two saddle-node bifurcations no longer occur at all (see Fig. 5h).

The bifurcation diagrams of Fig. 5 show not only the U and NU branches, but also record the fate of the branches of periodic orbits (when present) generated in Hopf bifurcations on the NU branch (Fig. 5a–f). For typical parameter values the NU branch is S-shaped, with the Hopf bifurcations occurring on the lower part. For example, a cut (not shown) at $\Lambda = 1$ barely crosses the locus of Hopf bifurcations but does so twice in quick succession indicating the presence of two Hopf bifurcations back to back (see Fig. 4); connecting these bifurcations is a stable branch of periodic orbits. With $\Lambda = 0.9$ (Fig. 5a) there is a period-doubling bifurcation on this original branch but the cascade (not shown) is incomplete (there are just two period-doublings followed by two reverse period-doublings).

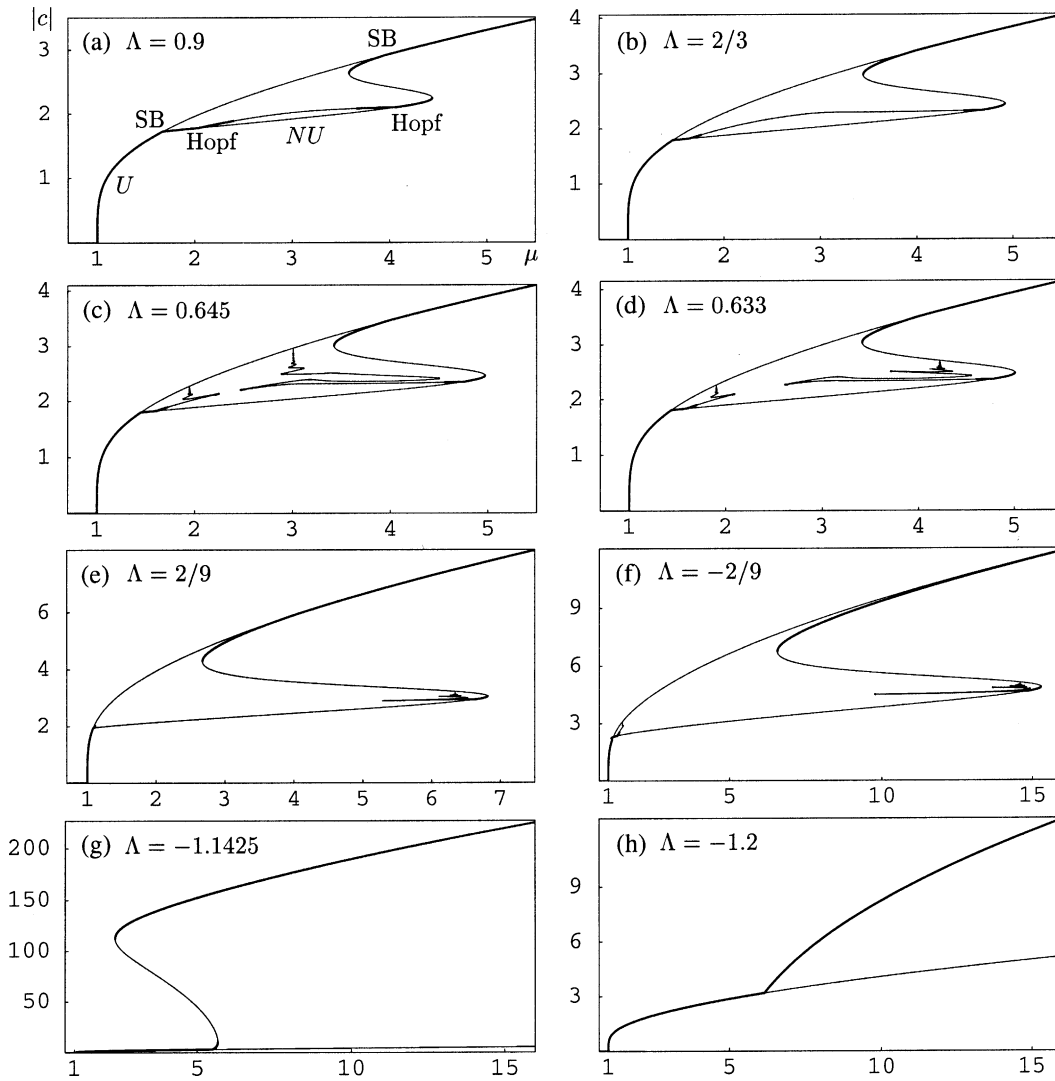


Fig. 5. Series of bifurcation diagrams, $|c| \equiv (|c_0|^2 + |c_1|^2)^{1/2}$ vs. μ , for different values of Λ . Stable (unstable) solutions are rendered with thick (thin) lines. Branches of periodic solutions originating in Hopf bifurcations are also shown.

Bifurcation “bubbles” of this type are familiar from problems related to the Shil’nikov bifurcation [32,33]. For $\Lambda = 2/3$ (Fig. 5b), the value corresponding to Fig. 6, there is (presumably) a complete period-doubling cascade and one can easily find a variety of periodic and chaotic attractors (see Fig. 6). Evidence that this cascade is not the whole story, however, is provided in Fig. 5c. The figure shows that, for $\Lambda = 0.645$, the branch of periodic orbits has split apart, each half terminating in a Shil’nikov-type homoclinic connection with the uniform state. The abruptness of this transition suggests the presence of other periodic orbits with which the original periodic branch is colliding. This interpretation is further supported by a second abrupt transition which occurs by $\Lambda = 0.633$ (Fig. 5d); the branch of periodic states produced in the second Hopf bifurcation (at $\mu \simeq 4.8$) now terminates in a homoclinic bifurcation on the NU states rather than the U states. As Λ is decreased even further (see Fig. 5e)

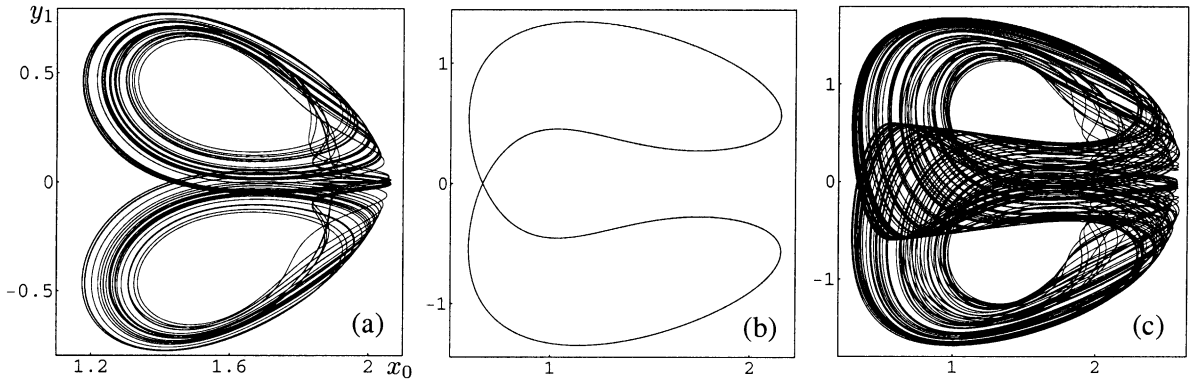


Fig. 6. Attractors for $\nu = 0$, $\alpha = 0.1$, $\Lambda = 2/3$ and (a) $\mu = 1.86$, (b) $\mu = 2.2$, and (c) $\mu = 2.5$.

the first homoclinic bifurcation (with the U state) moves very close to the initial Hopf bifurcation, occurring at $\mu \simeq 1.112$ when $\Lambda = 2/9$, while the second homoclinic bifurcation (on the NU branch) moves closer to the rightmost saddle-node bifurcation. The branch of periodic solutions corresponding to the former is almost invisible on the scale of the figure. A comparison of Fig. 5e and f shows that when Λ is small in magnitude the bifurcation diagrams on either side of $\Lambda = 0$ are qualitatively similar. The main differences are the change in scale (larger μ values for negative Λ) and the absence of the rightmost SB when $\Lambda < 0$: although the NU branch comes very close to the U branch for large μ the two branches remain distinct, in contrast to the situation for $\Lambda > 0$.

It turns out that the interesting periodic and chaotic behavior which one finds for values of Λ such as those used in Fig. 5b–f is associated with a *heteroclinic* bifurcation involving both O and U. The bifurcation sets for this global connection, $U \rightarrow O \rightarrow U$, are shown in Fig. 7. In this figure there are three curves of heteroclinic bifurcations which emerge from $(\mu, \Lambda) = (1, 0)$ into the region $\Lambda > 0$ and three that emerge into the region $\Lambda < 0$. For $\Lambda > 0$ two of these connect up smoothly forming a loop while the third oscillates back and forth an infinite number of times before terminating in a codimension-two heteroclinic bifurcation point at $(\mu, \Lambda) \simeq (2.5803, 0.1877)$. The heteroclinic cycle at this point involves all three types of fixed points: O, U, and the NU state between the two saddle-node bifurcations on the NU branch (see Section 4.2). For $\Lambda < 0$ the three curves of heteroclinic bifurcations remain separate (the upper two are almost indistinguishable on the scale of the figure). Two of them continue out to large values of μ (they have been followed to $\mu > 50$) while the third wiggles back and forth before terminating in another codimension-two heteroclinic cycle involving O, U, and NU. This point, $(\mu, \Lambda) \simeq (5.065, -0.159)$, is marked in Fig. 7 by a small circle; the wiggles are not visible on this scale. This point differs from the previous codimension-two point for $\Lambda > 0$ in a fundamental way because it involves the small amplitude NU state (after the first Hopf bifurcation) whose stable and unstable manifolds are each two-dimensional. We defer the details until Section 4 but, to summarize, the codimension-two heteroclinic cycle for $\Lambda > 0$ involves three points with one-dimensional unstable manifolds; the connection $O \rightarrow U$ is structurally stable (due to the invariance of the uniform plane) while the connections $U \rightarrow NU$ and $NU \rightarrow O$ are *each* of codimension-one. For $\Lambda < 0$ the connections $O \rightarrow U$ and $NU \rightarrow O$, are both structurally stable but the third, $U \rightarrow NU$, is *itself* of codimension-two.

Fig. 7 also shows the cut $\Lambda = 2/9$. This cut corresponds to the bifurcation diagram of Fig. 5e and crosses the heteroclinic bifurcation set four times. We use this Λ value to investigate further the dynamics associated with this bifurcation. Along this path the first Hopf bifurcation (at $\mu \simeq 1.106$) occurs almost immediately after the birth of the

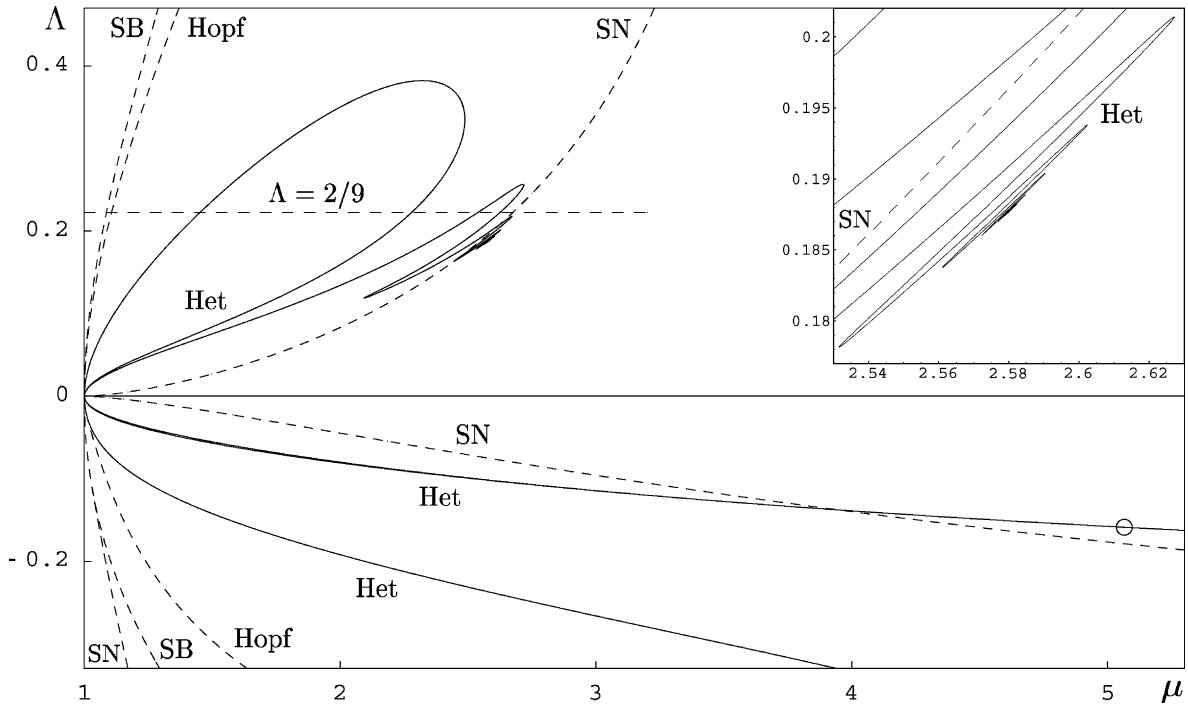


Fig. 7. Heteroclinic (Het) bifurcation sets (solid lines) representing the cycle $U \rightarrow O \rightarrow U$. The inset shows an enlargement of one of these curves near its termination in the codimension-two heteroclinic cycle $U \rightarrow NU \rightarrow O \rightarrow U$. Note that the cut $\Lambda = 2/9$ passes through four heteroclinic bifurcations.

NU branch (see Fig. 7). Between this Hopf bifurcation and the leftmost saddle-node bifurcation on the NU branch at $\mu \simeq 2.674$ there are no stable fixed points; in this region one can easily find chaotic attractors, such as those shown in Fig. 8, as well as a variety of interesting periodic solutions (see Fig. 9). Notice that the periodic orbits in Fig. 9 have \mathbb{Z}_2 symmetry, i.e. they are invariant under one of the reflections: $R_0, R_1, R_0 R_1$. Although these particular

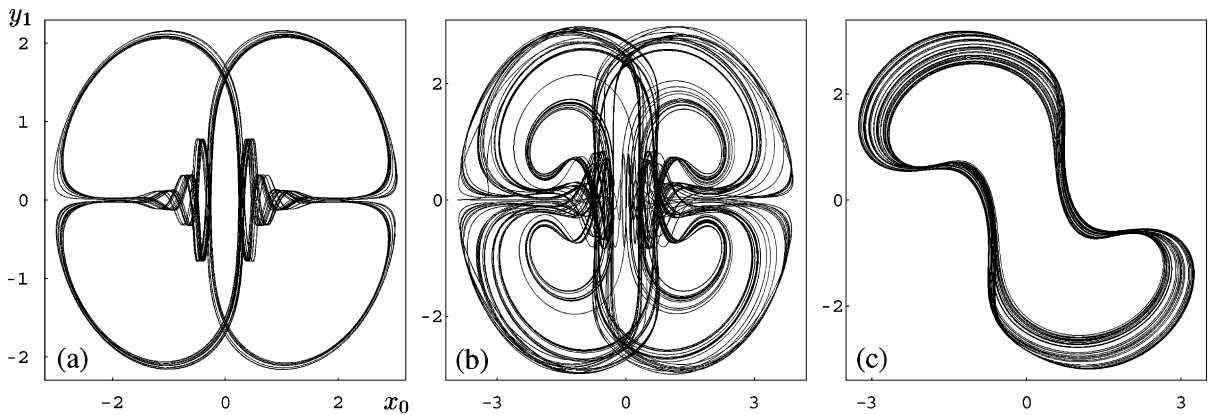


Fig. 8. Chaotic attractors for $\nu = 0, \alpha = 0.1, \Lambda = 2/9$ and (a) $\mu = 1.51$, (b) $\mu = 2.0$, and (c) $\mu = 2.54$.

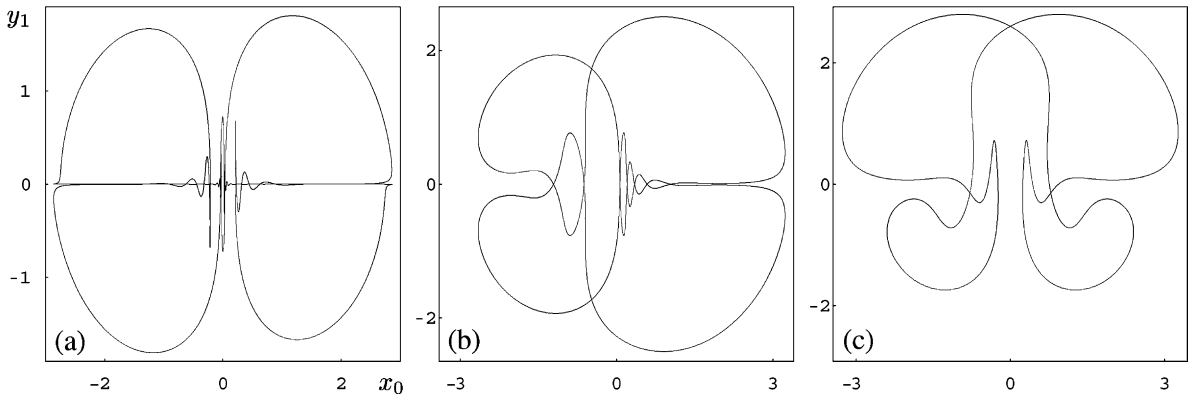


Fig. 9. \mathbb{Z}_2 -symmetric periodic attractors for $\nu = 0$, $\alpha = 0.1$, $\Lambda = 2/9$ and (a) $\mu = 1.41$, $R_0 R_1$ -symmetry; (b) $\mu = 1.64$, R_1 -symmetry; and (c) $\mu = 1.875$, R_0 -symmetry.

periodic orbits are somewhat exotic (in the sense that they do not belong to one of the basic families of periodic solutions analyzed below but resemble something like the ‘multi-pulse’ orbits identified in perturbations of the Hamiltonian problem) there are also sequences of simpler periodic orbits which come close to both O and U. These orbits, characterized by their symmetry (or lack thereof) and by the number of oscillations they experience near O, are related in a fundamental way to the heteroclinic connection $U \rightarrow O \rightarrow U$. A bifurcation diagram obtained by following many of these solutions numerically is displayed in Fig. 10, along with four representative orbits. This figure shows the period (half-period for symmetric orbits) as a function of μ . Two of the branches shown (the ones with lowest period) close on themselves to form isolas but most of the solutions terminate in homoclinic ($U_{\pm} \rightarrow U_{\pm}$) gluing bifurcations or heteroclinic ($U_{\pm} \rightarrow U_{\mp}$) symmetry-switching bifurcations. This is evident from the dramatic increase in period which occurs as the periodic orbits approach the fixed points. In the gluing bifurcations two asymmetric periodic orbits come together (using U_+ or U_-) to create a single R_1 -symmetric periodic orbit. In the symmetry-switching bifurcations two R_0 -symmetric periodic orbits transform (using both U_+ and U_-) into two $R_0 R_1$ -symmetric periodic orbits. In this second case the symmetry neither increases nor decreases but switches from one \mathbb{Z}_2 symmetry to another. Under appropriate conditions each of these processes is associated, as in the usual Shil’nikov scenario [33,34], with cascades of saddle-node and either period-doubling or symmetry-breaking bifurcations; the \mathbb{Z}_2 -symmetric branches undergo symmetry-breaking instead of period-doubling bifurcations since \mathbb{Z}_2 -symmetric periodic orbits do not (generically) have negative Floquet multipliers [35]. Note also that the way the two branches (e.g. an asymmetric and an R_1 -symmetric branch) merge with increasing period differs from that of the corresponding Shil’nikov problem in three dimensions with symmetry [36]. This is because the reflection symmetry in the latter case must be a complete inversion [34,37], while in our case the relevant symmetry R_1 is not (see Eq. (20)); in particular R_1 does not act on the swirling part of the flow near U_{\pm} in the plane $c_1 = 0$. In our case the two types of branches oscillate “in phase” around the homoclinic or heteroclinic points as their period increases (cf. Fig. 10), while they oscillate “out of phase” in the three-dimensional case with inversion symmetry. These differences between the standard situation and ours are a direct consequence of the fact that our two-mode truncation is four-dimensional, allowing new types of connection that are not possible in three dimensions. Note that in Fig. 10 we have only investigated the first two of the main heteroclinic bifurcations (recall that there are four such bifurcations when $\Lambda = 2/9$) and that there are *many* periodic solutions (e.g. those of Fig. 9) which have not been shown; these may form isolas or terminate at other, subsidiary, connections. In short, the full situation is extremely complex.

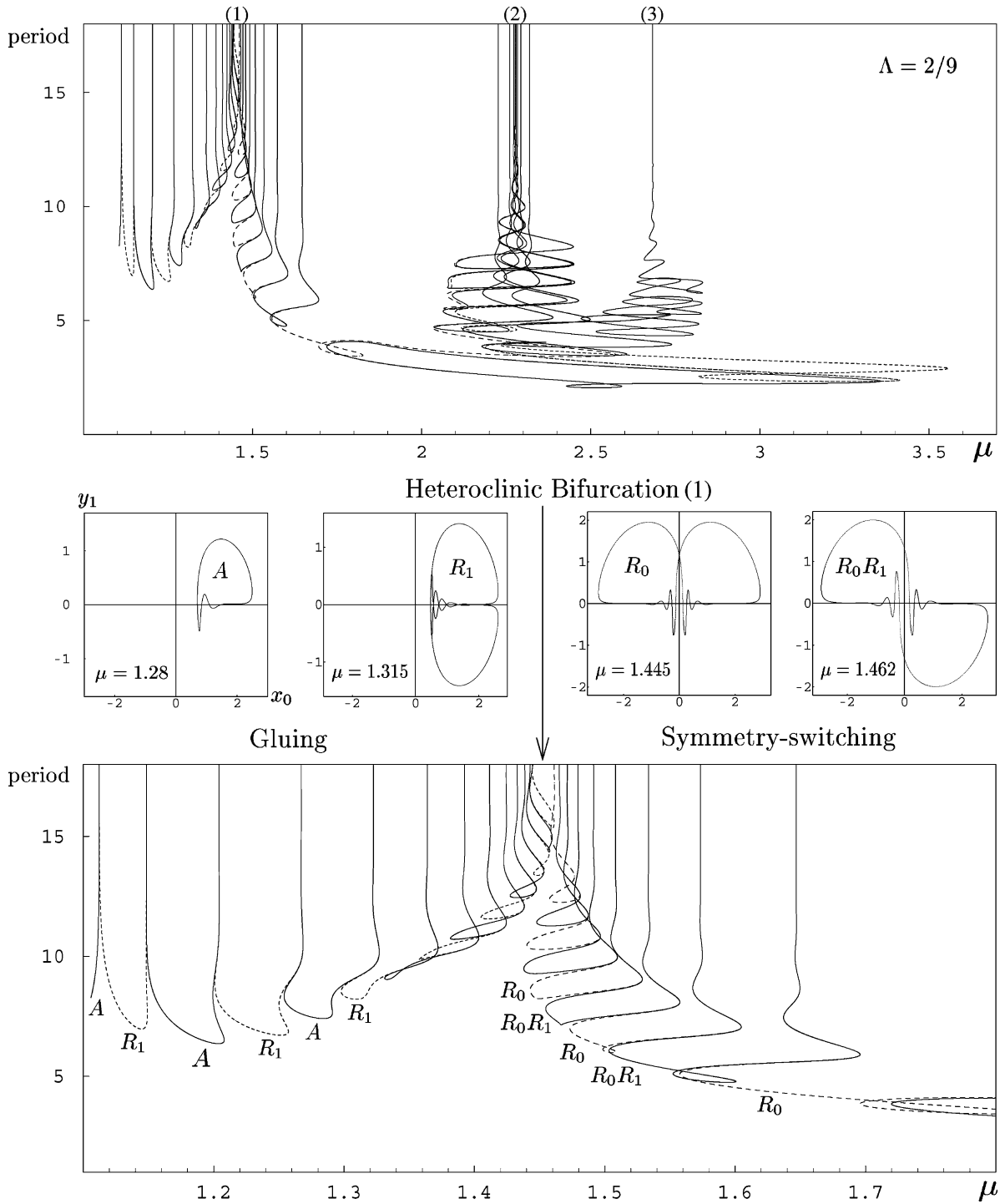


Fig. 10. Cascades of gluing ($A + A \leftrightarrow R_1$) and symmetry-switching ($R_0 + R_0 \leftrightarrow R_0R_1 + R_0R_1$) bifurcations for $\nu = 0$, $\alpha = 0.1$ and $\Lambda = 2/9$. These accumulate from opposite sides on the principal heteroclinic bifurcations, the first two of which, labeled (1) and (2), are shown (upper panel). At point (3) there is a homoclinic connection to NU. The lower panel shows an enlargement of the region near point (1). The diagrams show the period (half-period) of asymmetric (symmetric) periodic orbits as a function of μ .

4. Analysis

In this section we offer a geometric interpretation for the heteroclinic behavior observed in Eqs. (18) and (19) and use Poincaré return maps (cf. [33,38]) to analyze the global bifurcations responsible for it. Since heteroclinic cycles involve multiple connections they are in general difficult to observe unless the problem in question possesses a symmetry which preserves some of these connections. In Eqs. (18) and (19), the D_2 symmetry is responsible for the existence of the two invariant planes $c_1 = 0$ and $c_0 = 0$. Since there are no nontrivial solutions of the form $c_0 = 0$ this second invariant plane is of minimal consequence. The invariance of the space of spatially uniform solutions is, however, a property not only of Eqs. (18) and (19) but of the PDEs (7) and (8) as well, and this fact has a substantial influence on the dynamics of both systems. This is because once the trivial state O loses stability to U (for $\nu = 0$, $\Lambda \neq 0$ in a supercritical pitchfork bifurcation) the one-dimensional unstable manifold of O , $W^u(O)$, lies within the uniform plane $c_1 = 0$ and is therefore contained in the stable manifold of U , $W^s(U)$. This is because the states U_{\pm} are the only spatially uniform attractors of both the model and the PDEs. When U subsequently loses stability giving rise to the NU branch it acquires a one-dimensional unstable manifold, $W^u(U)$, which may, upon tuning a single parameter, intersect the three-dimensional stable manifold of O , $W^s(O)$. In this case there are structurally stable connections $O \rightarrow U_{\pm}$ (related by the symmetry R_0) which when combined with the structurally unstable connections $U_{\pm} \rightarrow O$ generate codimension-one heteroclinic cycles $U \rightarrow O \rightarrow U$. In this situation four symmetry-related cycles (excluding cycles with more than two segments) are simultaneously present (see Fig. 11), each associated with one of the four parts of $W^u(U)$. We denote these by $W^u_{\pm}(U_{\kappa})$, where $\kappa = \pm$, R_0 takes U_{κ} to $U_{-\kappa}$, and R_1 relates $W^u_{+}(U_{\kappa})$ to $W^u_{-}(U_{\kappa})$.

4.1. Heteroclinic bifurcation: $U \rightarrow O \rightarrow U$

To understand what happens in the neighborhood of the heteroclinic cycles $U \rightarrow O \rightarrow U$ it is useful to construct Poincaré return maps and study the fixed point solutions which correspond to periodic solutions of the original vector field. We proceed by first obtaining local maps from the linearized flow at O and U . Near O , the eigenvalues in the $c_0 = 0$ plane are complex and it is natural to use polar coordinates defined by $(x_1, y_1) = r(\cos \theta, \sin \theta)$.

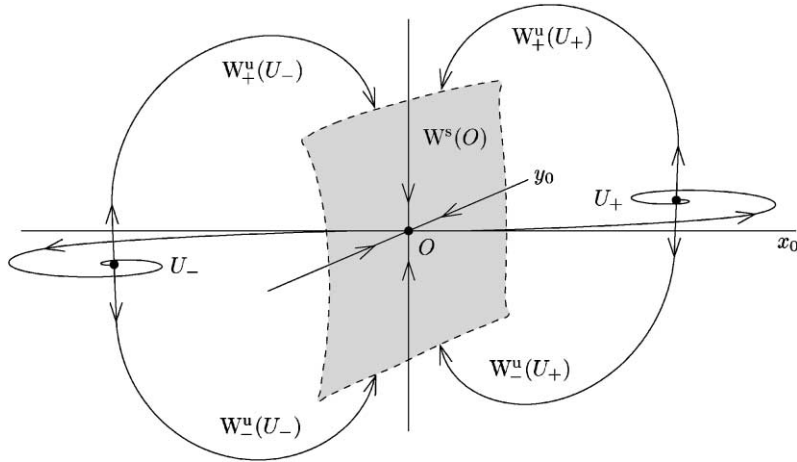


Fig. 11. Sketch of the codimension-one heteroclinic connection with the four cycles $U_{\pm} \rightarrow O \rightarrow U_{\pm}$.

We therefore write

$$\dot{x}_0 = \sigma x_0, \quad \dot{y}_0 = -\varrho y_0, \quad \dot{r} = -r, \quad \dot{\theta} = -\omega, \quad (24)$$

where $\sigma = \mu - 1 > 0$, $\varrho = \mu + 1$, and $\omega = 4\pi^2\alpha$ (see Section 2). Next we define appropriate Poincaré sections,

$$\Sigma_O : \{(x_0, y_0, r, \theta) | |x_0| \leq \epsilon, |y_0| \leq \epsilon, r = \epsilon\}, \quad \Sigma_O^\pm : \{(x_0, y_0, r, \theta) | x_0 = \pm\epsilon, |y_0| \leq \epsilon, r \leq \epsilon\},$$

and obtain the map $T_O : \Sigma_O \rightarrow \Sigma_O^+ \cup \Sigma_O^-$:

$$T_O : \begin{pmatrix} x_0 \\ y_0 \\ \epsilon \\ \theta \end{pmatrix} \mapsto \begin{pmatrix} \epsilon \operatorname{sign}(x_0) \\ y_0 \left| \frac{x_0}{\epsilon} \right|^{\varrho/\sigma} \\ \epsilon \left| \frac{x_0}{\epsilon} \right|^{1/\sigma} \\ \theta - \frac{\omega}{\sigma} \log \left| \frac{\epsilon}{x_0} \right| \end{pmatrix}. \quad (25)$$

Near the uniform fixed points U we assume $\mu > \sqrt{5}/2$ and therefore that the eigenvalues within the c_0 plane are complex conjugates, $-1 \pm i\Omega$. The other two eigenvalues, $s_1 > 0$ and $-s_2 < 0$, are taken to be real. One can then choose normal coordinates which satisfy

$$\dot{R} = -R, \quad \dot{\phi} = \Omega, \quad \dot{z} = s_1 z, \quad \dot{w} = -s_2 w. \quad (26)$$

Here we have again used a polar representation for two of the local variables (within the uniform plane) and, to simplify notation, the reflection R_0 has been absorbed into the definition of these coordinates; a point (R, ϕ, z, w) in the neighborhood of U_κ is mapped by R_0 to a point in the neighborhood of $U_{-\kappa}$ with exactly the same local coordinates. We next define the surfaces

$$\Sigma_U : \{(R, \phi, z, w) | R = \epsilon, |z| \leq \epsilon, |w| \leq \epsilon\}, \quad \Sigma_U^\pm : \{(R, \phi, z, w) | R \leq \epsilon, z = \pm\epsilon, |w| \leq \epsilon\},$$

and arrive at the local map $T_U : \Sigma_U \rightarrow \Sigma_U^+ \cup \Sigma_U^-$:

$$T_U : \begin{pmatrix} \epsilon \\ \phi \\ z \\ w \end{pmatrix} \mapsto \begin{pmatrix} \epsilon \left| \frac{z}{\epsilon} \right|^{1/s_1} \\ \phi + \frac{\Omega}{s_1} \log \left| \frac{\epsilon}{z} \right| \\ \epsilon \operatorname{sign}(z) \\ w \left| \frac{z}{\epsilon} \right|^{s_2/s_1} \end{pmatrix}. \quad (27)$$

Note that, by construction, this map is independent of κ .

The next step is to construct global maps by expanding about the exact heteroclinic cycle created when $W^u(U) \subset W^s(O)$. For convenience we introduce a rescaled bifurcation parameter λ , satisfying $\lambda = 0$ at the heteroclinic bifurcation, and write $W_\pm^u(U_\kappa) \cap \Sigma_O = (-\kappa\lambda, \kappa\bar{y}_0 + c\kappa\lambda, \epsilon, \bar{\theta} + d\lambda \pm \pi/2)$; $W^u(O) \cap \Sigma_U = (\epsilon, \bar{\phi}_h + b\lambda, 0, 0)$. Expanding to first order and taking into account the symmetries R_0 and R_1 leads to the maps $T_{O \rightarrow U_\kappa} : \Sigma_O^\kappa \rightarrow \Sigma_U$

and $T_{U_\kappa \rightarrow O}^\pm : \Sigma_U^\pm \rightarrow \Sigma_O$:

$$T_{O \rightarrow U_\kappa} : \begin{pmatrix} \kappa \epsilon \\ y_0 \\ r \\ \theta \end{pmatrix} \mapsto \begin{pmatrix} \epsilon \\ \bar{\phi}_h + A_1 \kappa y_0 + b\lambda \\ A_2 r \cos(\theta_2 + \theta) \\ A_3 r \cos(\theta_3 + \theta) \end{pmatrix}, \quad (28)$$

$$T_{U_\kappa \rightarrow O}^\pm : \begin{pmatrix} R \\ \phi \\ \pm \epsilon \\ w \end{pmatrix} \mapsto \begin{pmatrix} \kappa(B_1 R \cos(\phi_1 + \phi) \pm B_4 w - \lambda) \\ \kappa(\bar{y}_0 + B_2 R \cos(\phi_2 + \phi) \pm B_5 w + c\lambda) \\ \epsilon \\ \bar{\theta} \pm \frac{\pi}{2} + B_3 R \cos(\phi_3 + \phi) \pm B_6 w + d\lambda \end{pmatrix}. \quad (29)$$

Here, the symmetry R_1 is responsible for eliminating many of the terms in $T_{O \rightarrow U_\kappa}$ while the form of each map is also subject to requirements such as $T_{U_\kappa \rightarrow O}^+(R, \phi, \epsilon, w) = R_1 \circ T_{U_\kappa \rightarrow O}^-(R, \phi, -\epsilon, -w)$; near the origin $R_1(x_0, y_0, r, \theta) = (x_0, y_0, r, \theta + \pi)$. These maps, in appropriate combinations, can be used to study the many periodic solutions of Eqs. (18) and (19). We do not attempt to address all of the possibilities but concentrate on the prominent gluing and symmetry-switching bifurcations observed in Section 3. To do this we note that the first component ($x_0 = -\kappa\lambda$) of $W_\pm^u(U_\kappa) \cap \Sigma_O$ determines whether the next intersection is with Σ_O^+ or Σ_O^- . Specifically, if $\lambda < 0$, $W^u(U_\kappa)$ may intersect Σ_O^+ and return to a neighborhood of U_κ , but if $\lambda > 0$ (and small) then $W^u(U_\kappa)$ crosses Σ_O^- and subsequently visits the neighborhood of $U_{-\kappa}$. In other words, if $\lambda < 0$ there is the possibility of exact homoclinic connections, $U_\kappa \rightarrow (\text{neighborhood of } O) \rightarrow U_\kappa$, while if $\lambda > 0$ there is potential for exact heteroclinic connections, $U_\kappa \rightarrow (\text{neighborhood of } O) \rightarrow U_{-\kappa}$. In the first case homoclinic connections occur when $T_{O \rightarrow U_\kappa} \circ T_O \circ T_{U_\kappa \rightarrow O}^\pm(0, \phi, \pm\epsilon, 0) \in W^s(U_\kappa) \cap \Sigma_U$ while if $\lambda > 0$ the heteroclinic connections between U_κ and $U_{-\kappa}$ require $T_{O \rightarrow U_{-\kappa}} \circ T_O \circ T_{U_\kappa \rightarrow O}^\pm(0, \phi, \pm\epsilon, 0) \in W^s(U_{-\kappa}) \cap \Sigma_U$. Each of these conditions leads to the same equation

$$\sin\left(\tilde{\theta}_2 + d\lambda + \frac{\omega}{\sigma} \log|\lambda|\right) = 0, \quad (30)$$

where $\tilde{\theta}_2 = \theta_2 + \bar{\theta} - (\omega/\sigma) \log \epsilon$. The solutions of Eq. (30) are easy to visualize (see Fig. 12). There is an infinite cascade of homoclinic connections, $U_\kappa \rightarrow U_\kappa$, for $\lambda < 0$ and an infinite cascade of heteroclinic connections,

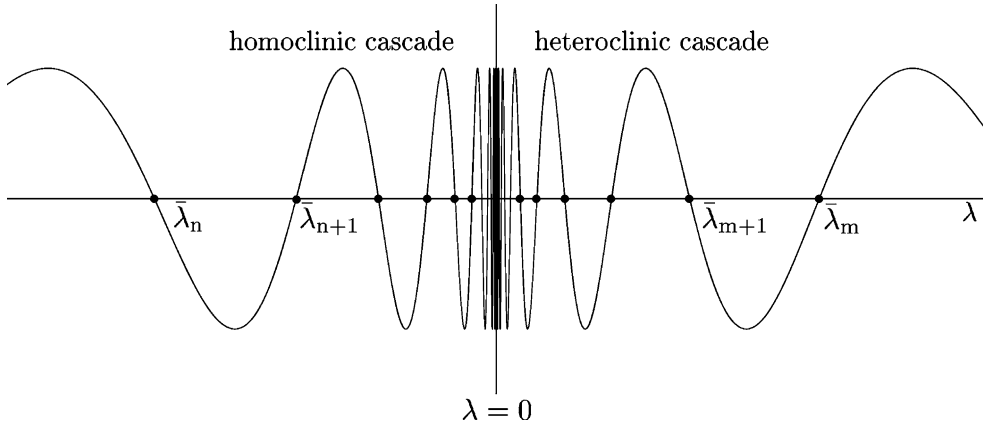


Fig. 12. Intersections with the horizontal axis, $\bar{\lambda}_n$ and $\bar{\lambda}_m$, give solutions to Eq. (30).

$U_\kappa \rightarrow U_{-\kappa}$, for $\lambda > 0$. Both series of parameters, $\bar{\lambda}_n < 0$ and $\bar{\lambda}_m > 0$, accumulate geometrically at $\lambda = 0$ with the scaling:

$$\lim_{n \rightarrow \infty} \frac{|\bar{\lambda}_{n+1}|}{|\bar{\lambda}_n|} = \lim_{m \rightarrow \infty} \frac{\bar{\lambda}_{m+1}}{\bar{\lambda}_m} = e^{-\pi\sigma/\omega}. \quad (31)$$

Note that this accumulation rate depends on the eigenvalues at the origin, and hence is nonuniversal.

To understand what happens near the n th homoclinic connection (at $\lambda = \bar{\lambda}_n < 0$) one can perform a local analysis by defining $\lambda = \bar{\lambda}_n + \tilde{\lambda}$, where $|\tilde{\lambda}| \ll |\bar{\lambda}_n|$. With $\tilde{\lambda}$ small enough, the time spent near the origin, O , can be neglected in comparison with the much larger amount of time spent near U_κ . This allows the composition $T_{O \rightarrow U_\kappa} \circ T_O \circ T_{U_\kappa \rightarrow O}^\pm$ to be replaced by a single map $T_{U_\kappa \rightarrow U_\kappa}^\pm : \Sigma_U^\pm \rightarrow \Sigma_U$ which comes from linearizing about $W_\pm^u(U_\kappa)$. Thus, after defining $W_\pm^u(U_\kappa) \cap \Sigma_U = (\epsilon, \bar{\phi} + e\tilde{\lambda}, \pm f\tilde{\lambda}, \pm \bar{w} \pm g\tilde{\lambda})$ we obtain

$$T_{U_\kappa \rightarrow U_\kappa}^\pm : \begin{pmatrix} R \\ \phi \\ \pm \epsilon \\ w \end{pmatrix} \mapsto \begin{pmatrix} \epsilon \\ \bar{\phi} + e\tilde{\lambda} + D_1 R \cos(\bar{\phi}_1 + \phi) \pm D_4 w \\ \pm(f\tilde{\lambda} + D_2 R \cos(\bar{\phi}_2 + \phi) \pm D_5 w) \\ \pm(\bar{w} + g\tilde{\lambda} + D_3 R \cos(\bar{\phi}_3 + \phi) \pm D_6 w) \end{pmatrix}. \quad (32)$$

The composition $T_{U_\kappa \rightarrow U_\kappa}^\pm \circ T_U$ defines a return map from Σ_U into itself. Fixed points of this map correspond to asymmetric periodic orbits of Eqs. (18) and (19) while R_1 -symmetric periodic orbits satisfy $T_{U_\kappa \rightarrow U_\kappa}^\pm \circ T_U(\epsilon, \phi, z, w) = (\epsilon, \phi, -z, -w)$. Both of these cases are described simultaneously by the equation

$$\pm|z| - f\tilde{\lambda} = \tilde{D}_2 |z|^{1/s_1} \cos\left(\tilde{\Phi}_2 - \frac{\Omega}{s_1} \log|z|\right) \pm \tilde{D}_5 |z|^{s_2/s_1}, \quad (33)$$

where

$$\tilde{D}_2 = \epsilon^{1-1/s_1} D_2, \quad \tilde{D}_5 = D_5 \bar{w} \epsilon^{-s_2/s_1}, \quad \tilde{\Phi}_2 = \bar{\phi}_2 + \bar{\phi} + \frac{\Omega}{s_1} \log \epsilon.$$

In deriving this expression we assumed $|z|, |\tilde{\lambda}| \ll \epsilon$. Eq. (33) is similar to the Shil'nikov equation [33,34] and depends critically on the magnitude of s_1 and s_2 . In fact Eq. (23) implies that $s_2 = 2 + s_1$, indicating that $s_2/s_1 > 1/s_1$ and hence that the last term in Eq. (33) becomes negligible compared with the first for sufficiently small $|z|$. In this case the condition $s_1 > 1$ guarantees that there are cascades of saddle-node, period-doubling, and symmetry-breaking bifurcations centered at $\tilde{\lambda} = 0$. For example, when $\Lambda = 2/9$ this condition is satisfied in the interval $1.123 \lesssim \mu \lesssim 3.960$. We construct the solutions of Eq. (33) in Fig. 13 by plotting separately the left-hand and right-hand sides of the equation. Intersections along the line with positive slope correspond to asymmetric

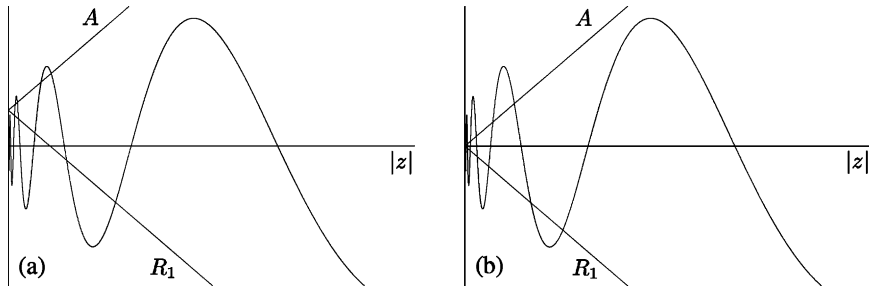


Fig. 13. Sketch of solutions to Eq. (33) indicating that both asymmetric and R_1 -symmetric periodic orbits are created in pairs. In case (a) $\tilde{\lambda} \neq 0$ there is an even (and finite) number of both types, while in (b) $\tilde{\lambda} = 0$ the numbers are infinite.

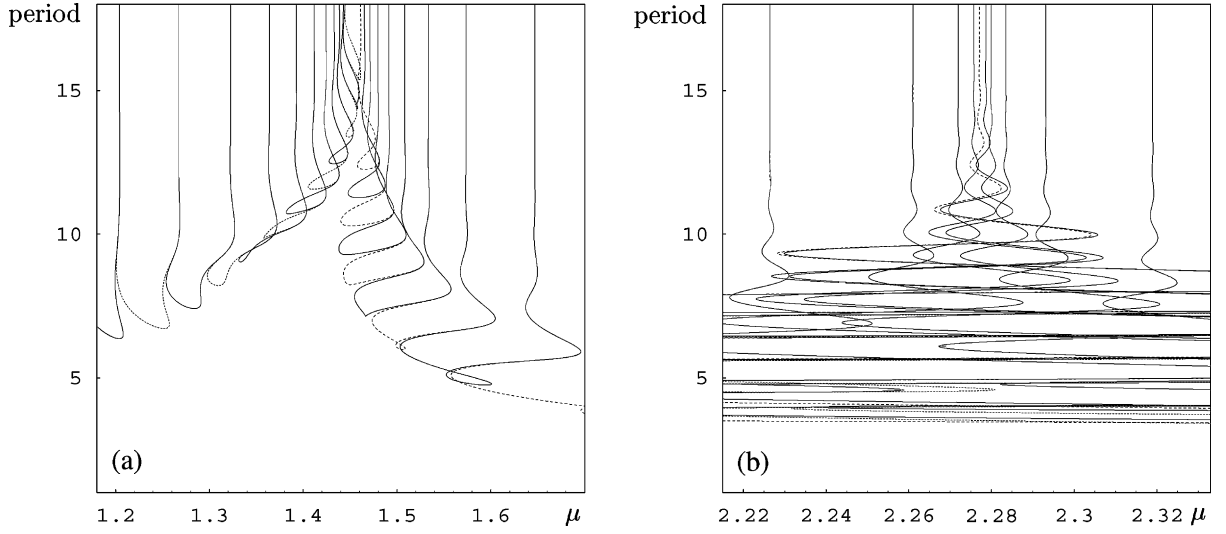


Fig. 14. Enlargements of the two gluing and symmetry-switching cascades from Fig. 10 illustrating the geometric scaling of Eq. (30).

solutions while those along the line of negative slope indicate R_1 -symmetric solutions. Note that these solutions are created, respectively, in quartets and pairs.

When $\lambda > 0$ one can concentrate on the neighborhood of the heteroclinic connections $U_\kappa \rightarrow U_{-\kappa}$ and perform the same type of analysis. In fact, the two cases are formally identical. The difference is that this time the “ \pm ” in Eq. (33) signifies R_0 - and R_0R_1 -symmetric periodic orbits, respectively. Thus, altogether, the analysis which led to Eqs. (30), (31) and (33) is consistent with the numerical results of Section 3. In particular, it predicts cascades of homoclinic ($\lambda < 0$) and heteroclinic ($\lambda > 0$) connections accumulating at the principal heteroclinic bifurcation ($\lambda = 0$). These can be identified as the gluing and symmetry-switching bifurcations shown in Fig. 10. When $\lambda < 0$ the periodic solutions created are alternately asymmetric and R_1 -symmetric while if $\lambda > 0$ the symmetry switches between R_0 and R_0R_1 . Furthermore, each of these associated connections can contain (for $s_1 > 1$) dynamics of Shil’nikov type and its attendant chaos. The scaling predicted by Eq. (30), approximately 0.70 and 0.36 for the heteroclinic bifurcations at $\mu \simeq 1.455$ and 2.278, respectively, can be compared with Fig. 14 which shows enlargements of the two cascades in Fig. 10. Direct measurement from this figure yields ratios of 0.69 and 0.35 which are in excellent agreement with Eq. (30). In addition, Eq. (33) leads to a prediction for the scaling of individual saddle-node cascades:

$$\lim_{k \rightarrow \infty} \frac{\tilde{\lambda}_{k+1}}{\tilde{\lambda}_k} = -e^{-\pi/\Omega}, \quad (34)$$

where the saddle-node bifurcations, on alternating sides (of, e.g. $\tilde{\lambda}_n$), have been denoted by $\tilde{\lambda}_k$. Eq. (34) gives values of -0.1853 at $\mu \simeq 1.455$ and -0.4534 at $\mu \simeq 2.278$; this is also consistent with Fig. 14 and the fact that in the second cascade (Fig. 14b) the saddle-node bifurcations are considerably more prominent than in the first.

4.2. Codimension-two point: $U \rightarrow NU \rightarrow O \rightarrow U$

Fig. 7 shows that for positive Λ one of the curves marking heteroclinic bifurcations terminates at $(\mu, \Lambda) \simeq (2.5803, 0.1877)$. This value of μ falls between the two saddle-node bifurcations on the NU branch; three distinct

NU solutions are therefore present (see Fig. 5e). One of these is stable and cannot be involved in heteroclinic dynamics while the lower branch after the Hopf bifurcation has a two-dimensional stable and a two-dimensional unstable manifold. The third NU state, NU_0 , lying between the two saddle-node bifurcations has a three-dimensional stable manifold $W^s(\text{NU}_0)$ and a one-dimensional unstable manifold $W^u(\text{NU}_0)$, and can therefore participate in the simplest heteroclinic connections involving either O or U. Since the intersection of $W^u(\text{U})$ (one-dimensional) with $W^s(\text{NU}_0)$ is of codimension-one the locus of connections $\text{U} \rightarrow \text{NU}_0$ is represented by a curve in the (μ, Λ) plane. Likewise, the intersection of $W^u(\text{NU}_0)$ with $W^s(\text{O})$ (three-dimensional) is also of codimension-one and so is represented by a second curve in the (μ, Λ) plane. Generically, these two curves intersect, and the point of intersection corresponds to a heteroclinic cycle of the type $\text{U} \rightarrow \text{NU} \rightarrow \text{O} \rightarrow \text{U}$. In the neighborhood of such a codimension-two point one can again use Poincaré maps to study nearby periodic solutions and related bifurcations. We focus first on the curve of heteroclinic bifurcations $\text{U} \rightarrow \text{O} \rightarrow \text{U}$ (see Fig. 7) which appears to emanate from this sort of intersection. We assume that the NU state of interest, NU_0 (hereafter simply NU), is hyperbolic with two real eigenvalues (one stable, and one unstable) and two complex eigenvalues (both stable). This is the case when $(\mu, \Lambda) \simeq (2.5803, 0.1877)$. Near NU we can therefore find normal coordinates (u, v, ρ, ψ) satisfying

$$\dot{u} = \beta u, \quad \dot{v} = -\gamma v, \quad \dot{\rho} = -\delta \rho, \quad \dot{\psi} = \varpi. \quad (35)$$

Here β , γ , and δ are positive and unrelated to the earlier variables of the same names. We define next the Poincaré sections

$$\Sigma_{\text{NU}} : \{(u, v, \rho, \psi) | |u| \leq \epsilon, |v| \leq \epsilon, \rho = \epsilon\}, \quad \Sigma_{\text{NU}}^{\pm} : \{(u, v, \rho, \psi) | u = \pm\epsilon, |v| \leq \epsilon, \rho \leq \epsilon\},$$

and obtain the map $T_{\text{NU}} : \Sigma_{\text{NU}} \rightarrow \Sigma_{\text{NU}}^+ \cup \Sigma_{\text{NU}}^-$:

$$T_{\text{NU}} : \begin{pmatrix} u \\ v \\ \epsilon \\ \psi \end{pmatrix} \mapsto \begin{pmatrix} \epsilon \operatorname{sign}(u) \\ v \left| \frac{u}{\epsilon} \right|^{\gamma/\beta} \\ \epsilon \left| \frac{u}{\epsilon} \right|^{\delta/\beta} \\ \psi + \frac{\varpi}{\beta} \log \left| \frac{\epsilon}{u} \right| \end{pmatrix}. \quad (36)$$

Although there are four symmetry-related NU states, we have once again absorbed the symmetries (R_0 and R_1) into the definition of the local variables (u, v, ρ, ψ) . The map T_{NU} lacks any explicit dependence on the sign of its absolute coordinates. It will sometimes be necessary, nonetheless, to distinguish the four symmetry-related states; we do this with the notation, NU_{κ}^{\pm} . Here NU_{+}^{+} is associated with $W_{+}^u(\text{U}_{+})$ and the symmetries act according to $R_0(\text{NU}_{\kappa}^{\pm}) = \text{NU}_{-\kappa}^{\pm}$, $R_1(\text{NU}_{\kappa}^{\pm}) = \text{NU}_{\kappa}^{\mp}$. Furthermore, we can assume without loss of generality that any trajectory approaching O after leaving NU crosses Σ_{NU}^{+} . Trajectories which cross Σ_{NU}^{-} are lost (they may, e.g. be attracted to the stable NU state). We can now expand about the exact heteroclinic cycle at the codimension-two point to obtain two global maps, $T_{\text{U}_{\kappa} \rightarrow \text{NU}_{\kappa}^{\pm}} : \Sigma_{\text{U}}^{\pm} \rightarrow \Sigma_{\text{NU}}$ and $T_{\text{NU}_{\kappa}^{\pm} \rightarrow \text{O}} : \Sigma_{\text{NU}}^{\pm} \rightarrow \Sigma_{\text{O}}$:

$$T_{\text{U}_{\kappa} \rightarrow \text{NU}_{\kappa}^{\pm}} : \begin{pmatrix} R \\ \phi \\ \pm\epsilon \\ w \end{pmatrix} \mapsto \begin{pmatrix} E_1 R \cos(\tilde{\phi}_1 + \phi) \pm E_4 w + \lambda_1 \\ \bar{v} + E_2 R \cos(\tilde{\phi}_2 + \phi) \pm E_5 w + e\lambda_1 + f\lambda_2 \\ \epsilon \\ \bar{\psi} + E_3 R \cos(\tilde{\phi}_3 + \phi) \pm E_6 w + g\lambda_1 + h\lambda_2 \end{pmatrix}, \quad (37)$$

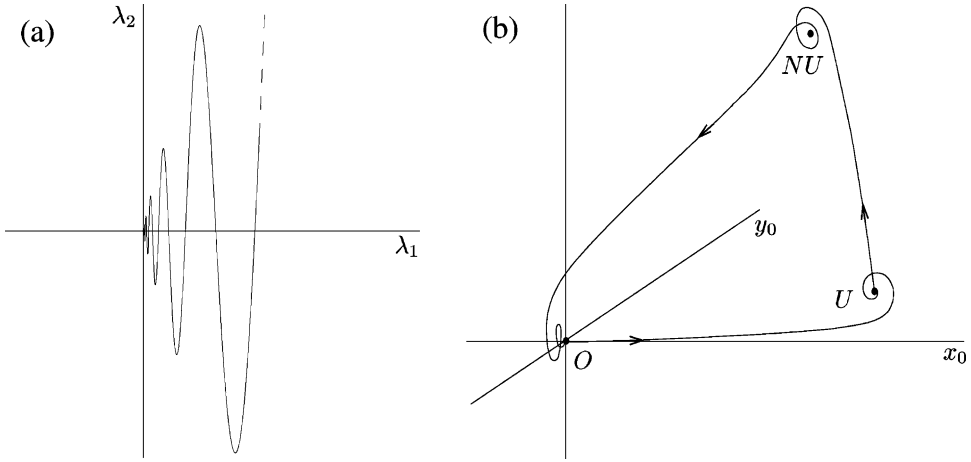


Fig. 15. (a) Bifurcation set for the heteroclinic cycle $U \rightarrow O \rightarrow U$ in the (λ_1, λ_2) plane. (b) Sketch of a heteroclinic cycle at a particular point along this curve.

$$T_{NU_k^\pm \rightarrow O} : \begin{pmatrix} \epsilon \\ v \\ \rho \\ \psi \end{pmatrix} \mapsto \begin{pmatrix} \kappa (G_1 \rho \cos(\psi_1 + \psi) + G_4 v + \lambda_2) \\ \kappa (\hat{y}_0 + G_2 \rho \cos(\psi_2 + \psi) + G_5 v + l\lambda_1 + m\lambda_2) \\ \epsilon \\ \hat{\theta} \pm \frac{\pi}{2} + G_3 \rho \cos(\psi_3 + \psi) + G_6 v + p\lambda_1 + q\lambda_2 \end{pmatrix}. \quad (38)$$

Here \bar{v} , $\bar{\psi}$, \hat{y}_0 , and $\hat{\theta}$ are parameters determined by the location of the exact heteroclinic cycle(s) at $(\lambda_1, \lambda_2) = (0, 0)$ while λ_1 and λ_2 are linear combinations of μ and Λ measuring the distance from the codimension-two point. Note that because of the way they have been chosen, λ_1 controls the breaking of the connection $U \rightarrow NU$ while a nonzero λ_2 breaks the connection $NU \rightarrow O$. In other words, the λ_1 and λ_2 axes are precisely the bifurcation sets for the heteroclinic connections $NU \rightarrow O$ and $U \rightarrow NU$, respectively.

The goal of explaining Fig. 7 prompts us to look for exact heteroclinic connections of the form $U \rightarrow (\text{neighborhood of } NU) \rightarrow O \rightarrow U$ (see Fig. 15b). This can be done, for example, by starting on $W_+^u(U_+) \cap \Sigma_U^+ = (0, \phi, \epsilon, 0)$ and requiring that the composition $T_{NU_+^\pm \rightarrow O} \circ T_{NU} \circ T_{U_+ \rightarrow NU_+^\pm}$ maps this point somewhere within $W^s(O)$. Such a prescription leads to the equation

$$\lambda_2 + \tilde{G}_1 \lambda_1^{\delta/\beta} \cos \left(\tilde{\psi} + g\lambda_1 + h\lambda_2 - \frac{\varpi}{\beta} \log \lambda_1 \right) + \tilde{G}_4 (\bar{v} + e\lambda_1 + f\lambda_2) \lambda_1^{\gamma/\beta} = 0, \quad (39)$$

with λ_1 positive and

$$\tilde{G}_1 = \epsilon^{1-\delta/\beta} G_1, \quad \tilde{G}_4 = \epsilon^{-\gamma/\beta} G_4, \quad \tilde{\psi} = \psi_1 + \bar{\psi} + \frac{\varpi}{\beta} \log \epsilon.$$

The curve defined by Eq. (39) has been plotted in Fig. 15a (cf. Fig. 7) using the numerical values $\beta \simeq 1.204$, $\gamma \simeq 3.206$, $\delta = 1$, and $\varpi \simeq 7.454$ obtained from the eigenvalues of the relevant NU state at $(\mu, \Lambda) \simeq (2.5803, 0.1877)$, and arbitrary choices for the remaining parameters. In Fig. 15b we sketch the simplest kind (asymmetric, two segments) of heteroclinic cycle along this curve. We identify the oscillations in the (λ_1, λ_2) plane with those along the curve of heteroclinic cycles $U \rightarrow O \rightarrow U$ in Fig. 7 near the codimension-two point.

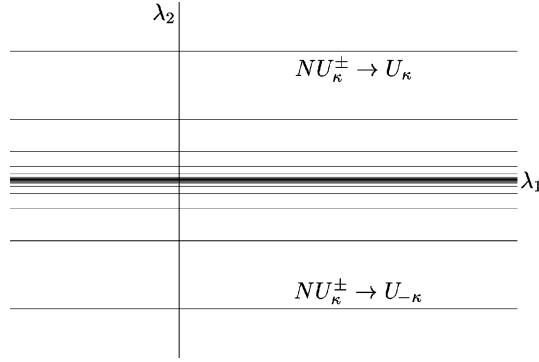


Fig. 16. Bifurcation sets for the heteroclinic connections $NU \rightarrow U$ accumulating on the λ_1 axis, the locus of the connections $NU \rightarrow O \rightarrow U$.

Although an analysis of the codimension-two point $U \rightarrow NU \rightarrow O \rightarrow U$ has been successful in explaining several features of Fig. 7 this bifurcation point is also the organizing center for a great deal of additional dynamics. We begin a more thorough exploration by recalling that the λ_1 axis represents the heteroclinic connection $NU \rightarrow O$. At a small but finite distance away from that axis the connection is broken. However, because of the structurally stable connection $O \rightarrow U$ the unstable manifold of NU is propelled, after missing O , toward the neighborhood of either U_+ or U_- ; this suggests the possibility of additional connections $NU \rightarrow U$. Furthermore, from the map $T_{NU_\kappa^\pm \rightarrow O}$ one can see that heteroclinic connections of the form $NU_\kappa^\pm \rightarrow U_\kappa$ are only possible if $\lambda_2 > 0$ while the other kind, $NU_\kappa^\pm \rightarrow U_{-\kappa}$, require $\lambda_2 < 0$. To search for such connections we start on $W^u(NU)$ and apply the condition: $T_{O \rightarrow U_{\varepsilon\kappa}} \circ T_O \circ T_{NU_\kappa^\pm \rightarrow O}(\epsilon, 0, 0, \psi) \in W^s(U) \cap \Sigma_U$, where $\varepsilon = \text{sign}(\lambda_2)$. This leads to the equation (cf. Eq. (30)):

$$\sin\left(\hat{\theta}_2 + p\lambda_1 + q\lambda_2 + \frac{\omega}{\sigma}\log|\lambda_2|\right) = 0, \quad (40)$$

where $\hat{\theta}_2 = \theta_2 + \hat{\theta} - (\omega/\sigma)\log\epsilon$. The solutions are sketched (for small λ_1, λ_2) in Fig. 16. Note that there are an infinite number of curves representing each connection and that these accumulate with the scaling of Eq. (31), $\exp(-\pi\sigma/\omega)$, on the λ_1 axis from either side. What makes these curves interesting is the fact that they cross the λ_2 axis. Whenever this happens there are codimension-two heteroclinic cycles. For $\lambda_2 > 0$ these take the form $U_\kappa \rightarrow NU_\kappa^\pm \rightarrow U_\kappa$ while for $\lambda_2 < 0$ the cycles $U_\kappa \rightarrow NU_\kappa^\pm \rightarrow U_{-\kappa} \rightarrow NU_{-\kappa}^\pm \rightarrow U_\kappa$ alternate between U_+ and U_- (i.e. they have R_0 or R_0R_1 symmetry). Thus, associated with the original codimension-two point ($U \rightarrow NU \rightarrow O \rightarrow U$) are cascades of additional codimension-two points ($U \rightarrow NU \rightarrow U$) which have their own dynamical consequences. To pursue this issue, we focus (for $\lambda_2 > 0$) on one of these points, say $(\lambda_1, \lambda_2) = (0, \bar{\lambda}_2)$, and perform a local analysis by setting $\lambda_2 = \bar{\lambda}_2 + \tilde{\lambda}_2$ with $|\tilde{\lambda}_2| \ll \bar{\lambda}_2$. If $\tilde{\lambda}_2$ is small enough then trajectories come much closer to U and NU than they do to O . It is thus advantageous to neglect the origin and use a new global map, $T_{NU_\kappa^\pm \rightarrow U_\kappa} : \Sigma_{NU}^+ \rightarrow \Sigma_U$, given by

$$T_{NU_\kappa^\pm \rightarrow U_\kappa} : \begin{pmatrix} \epsilon \\ v \\ \rho \\ \psi \end{pmatrix} \mapsto \begin{pmatrix} \epsilon \\ \hat{\phi} + \hat{b}\lambda_1 + \hat{c}\tilde{\lambda}_2 + H_1\rho \cos(\hat{\psi}_1 + \psi) + H_4v \\ \pm(\hat{d}\tilde{\lambda}_2 + H_2\rho \cos(\hat{\psi}_2 + \psi) + H_5v) \\ \pm(\hat{w} + \hat{e}\lambda_1 + \hat{f}\tilde{\lambda}_2 + H_3\rho \cos(\hat{\psi}_3 + \psi) + H_6v) \end{pmatrix}. \quad (41)$$

This new map in combination with T_U , T_{NU} , and $T_{U_\kappa \rightarrow NU_\kappa^\pm}$ allows, among other things, the determination of additional (codimension-one) bifurcation curves. For example, breaking the connection $U \rightarrow NU$ may lead (for

$\lambda_1 > 0$) to homoclinic orbits, $U_\kappa \rightarrow U_\kappa$. Finding these homoclinic bifurcation sets is equivalent to finding points $(0, \phi, \epsilon, 0) \in W_+^u(U_\kappa) \cap \Sigma_U^+$ which are mapped to $W^s(U_\kappa)$ under $T_{NU_\kappa^+ \rightarrow U_\kappa} \circ T_{NU} \circ T_{U_\kappa \rightarrow NU_\kappa^+}$. Such points satisfy the equation

$$\hat{d}\tilde{\lambda}_2 + \hat{H}_2\lambda_1^{\delta/\beta} \cos\left(\hat{\psi}_2 + g\lambda_1 + h\tilde{\lambda}_2 - \frac{\varpi}{\beta}\log\lambda_1\right) + \hat{H}_5(\hat{v} + e\lambda_1 + f\tilde{\lambda}_2)\lambda_1^{\gamma/\beta} = 0, \quad (42)$$

where λ_1 must be positive, and

$$\hat{H}_2 = H_2\epsilon^{1-\delta/\beta}, \quad \hat{\psi}_2 = \hat{\psi}_2 + \hat{\psi} + h\tilde{\lambda}_2 + \frac{\varpi}{\beta}\log\epsilon, \quad \hat{v} = \bar{v} + f\tilde{\lambda}_2, \quad \hat{H}_5 = H_5\epsilon^{-\gamma/\beta}.$$

Eq. (42) is virtually identical in form to Eq. (39) and defines a curve in the $(\lambda_1, \tilde{\lambda}_2)$ plane which is well represented by Fig. 15a under the substitution $\lambda_2 \rightarrow \tilde{\lambda}_2$.

The other way of breaking the cycle $U_\kappa \rightarrow NU_\kappa^\pm \rightarrow U_\kappa$ (i.e. perturbing the connection $NU \rightarrow U$) provides two more possibilities for codimension-one cycles: $NU_\kappa^\pm \rightarrow NU_\kappa^\pm$ and $NU_\kappa^\pm \rightarrow NU_\kappa^\mp \rightarrow NU_\kappa^\pm$. These cycles can be located, for example, by looking at NU_κ^+ and subjecting a point $(\epsilon, 0, 0, \psi) \in W^u(NU) \cap \Sigma_{NU}^+$ to the requirement $T_{U_\kappa \rightarrow NU_\kappa^+} \circ T_U \circ T_{NU_\kappa^+ \rightarrow U_\kappa}(\epsilon, 0, 0, \psi) \in W^s(NU)$. Here $\epsilon = \text{sign}(\hat{d}\tilde{\lambda}_2)$, reflecting the fact that it is the parameter $\tilde{\lambda}_2$ which determines whether the connection $NU_\kappa^+ \rightarrow U_\kappa$ breaks ‘up’ or ‘down’. Both cases are described by the equation

$$\lambda_1 + \hat{E}_1|\tilde{\lambda}_2|^{1/s_1} \cos\left(\hat{\phi}_1 + \hat{b}\lambda_1 + \hat{c}\tilde{\lambda}_2 - \frac{\Omega}{s_1}\log|\tilde{\lambda}_2|\right) + \epsilon\hat{E}_4\left(\hat{w} + \hat{e}\lambda_1 + \hat{f}\tilde{\lambda}_2\right)|\tilde{\lambda}_2|^{s_2/s_1} = 0, \quad (43)$$

where

$$\hat{E}_1 = E_1\epsilon\left|\frac{\hat{d}}{\epsilon}\right|^{1/s_1}, \quad \hat{\phi}_1 = \tilde{\phi}_1 + \hat{\phi} + \frac{\Omega}{s_1}\log\left(\frac{\epsilon}{\tilde{\lambda}_2}\right), \quad \hat{E}_4 = E_4\left|\frac{\hat{d}}{\epsilon}\right|^{s_2/s_1}.$$

This equation is analogous to Eqs. (39) and (42) except that now the ‘independent’ variable is $\tilde{\lambda}_2$ and may be either positive or negative. We remark that the other cascade ($\lambda_2 < 0$) of codimension-two points can be treated in a similar manner. The required map $T_{NU_\kappa^\pm \rightarrow U_\kappa}$ is of the same form as $T_{NU_\kappa^\pm \rightarrow U_\kappa}$ given above (the parameters will take different values, of course) and the relevant codimension-one connections (which imply cycles) are also completely analogous. Eq. (42), with appropriate reinterpretation, describes the bifurcation set for $U_\kappa \rightarrow U_{-\kappa}$ while the connections $NU_\kappa^\pm \rightarrow NU_{-\kappa}^\pm$ and $NU_\kappa^\pm \rightarrow NU_{-\kappa}^\mp$ correspond to solutions of Eq. (43). We illustrate the full situation predicted by the Poincaré maps in Fig. 17. This can be compared with Fig. 18 which shows many of the same bifurcation sets obtained from Eqs. (18) and (19). Here we have continued, in μ and Λ , the first three gluing bifurcations of Fig. 10 (at $\mu \simeq 1.112, 1.149$, and 1.204) and the first three symmetry-switching bifurcations (at $\mu \simeq 1.647, 1.573$, and 1.533). Because the symmetry-switching bifurcations are bounded by a curve of heteroclinic bifurcations they form closed curves and do not reach the region of the codimension-two point $(\mu, \Lambda) \simeq (2.5803, 0.1877)$ (there are presumably others, below the oscillating curve of heteroclinic bifurcations, which do). However, the three gluing bifurcations ($U_\kappa \rightarrow U_\kappa$) terminate at three of the codimension-two points ($U \rightarrow NU \rightarrow U$) identified above. Evidence of this is provided by following the connections $U \rightarrow NU$ (close to the set of saddle-node bifurcations in Fig. 18), as well as $NU \rightarrow O$, and $NU_\kappa^\pm \rightarrow U_\kappa$ (only three of the latter are shown). It is clear that the cascades of this section and of Section 4.1 are not independent. The cascade of gluing bifurcations associated with the principal heteroclinic bifurcation $U \rightarrow O \rightarrow U$ terminates in the cascade of codimension-two cycles $U \rightarrow NU \rightarrow U$ associated with the main codimension-two point $U \rightarrow NU \rightarrow O \rightarrow U$.

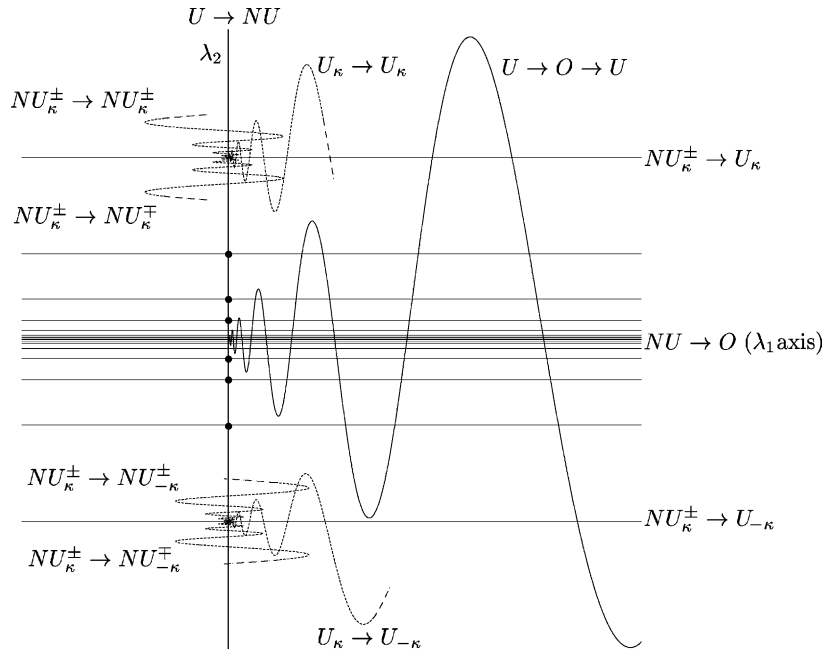


Fig. 17. Dynamics near the codimension-two point $U \rightarrow NU \rightarrow O \rightarrow U$. A curve of heteroclinic cycles $U \rightarrow O \rightarrow U$ emerges from $(\lambda_1, \lambda_2) = (0, 0)$ while three separate curves (dotted) of homoclinic or heteroclinic cycles are generated at each of the associated codimension-two points (solid dots) $U \rightarrow NU \rightarrow U$.

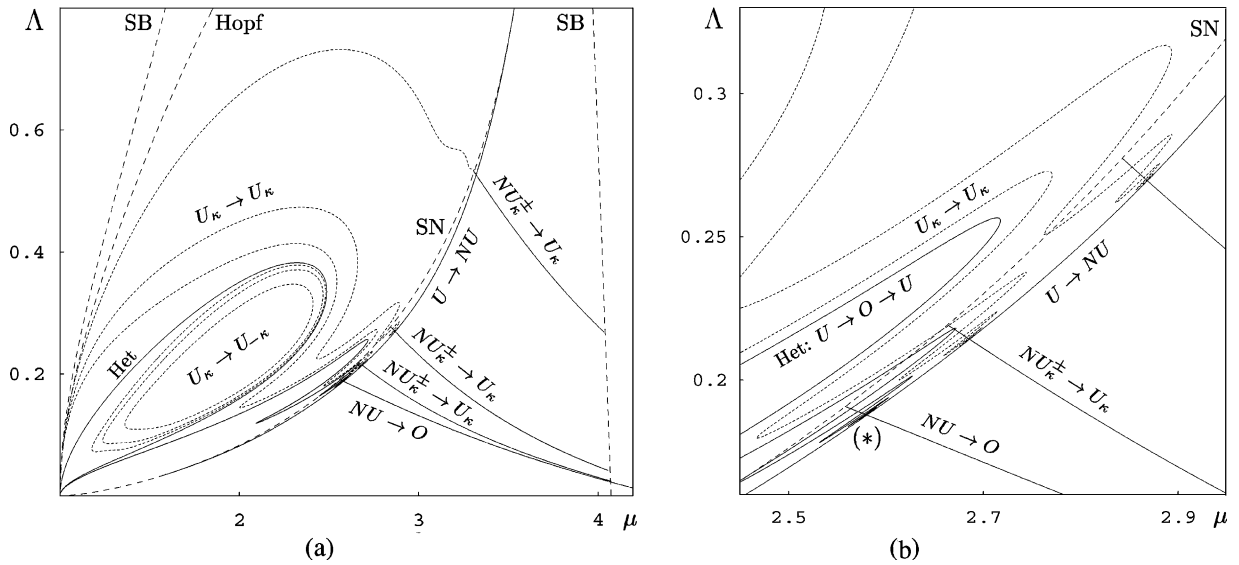


Fig. 18. Additional global bifurcation sets for Eqs. (18) and (19) including three gluing ($U_\kappa \rightarrow U_\kappa$) and three symmetry-switching ($U_\kappa \rightarrow U_{-\kappa}$) bifurcations (dotted lines). (b) Enlargement near the codimension-two point (*): $U \rightarrow NU \rightarrow O \rightarrow U$.

5. Comparison with the PDEs

Since it is the dynamics of the PDEs that are of ultimate interest, one would like to understand how faithfully their behavior is represented by a truncated set of ODEs. While there is no a priori reason to assume that a finite number of modes can accurately capture the effect of the nonlinear terms, it turns out that in many problems they do [17,20,27]. To investigate this question we have integrated the PDE system (7)–(8) using fast Fourier transforms (FFTs) in space and a fourth-order Runge–Kutta method in time. Starting with random initial conditions, we find that attractors for Eqs. (7) and (8) are frequently reflection-symmetric (in x) and as such are well described by restricting to the cosine subspace. Whenever this is the case we have used initial conditions close to the cosine subspace for ease of comparison with the results from the ODEs. In addition, numerical simulations of Eqs. (7) and (8) indicate that the influence of the higher modes is often negligible, particularly for periodic orbits and chaotic attractors which are approximately heteroclinic. Fig. 19 shows that this heteroclinic behavior, described in Sections 2–4 within the two-mode model (18)–(19), also occurs in the full PDEs.

To examine the influence of higher modes ($n > 1$) on the dynamics we have computed $|c_0|$, $|c_1|$, and $\sum_{n=2}^N |c_n|$ as functions of time, after first allowing transients to die away. The solutions in Fig. 20 represent typical chaotic attractors that can be found for $\Lambda = 2/9$ and $1.5 \lesssim \mu \lesssim 2.8$, together with the time series representing their harmonic content. Notice that in all cases the amplitude of the higher modes (thick lines in the right-hand set of panels) remains small, indicating that these modes do not play a significant role in the dynamics.

While such a low-dimensional description is not unexpected for small amplitudes (i.e. near onset at $\mu = 1$) Eqs. (7) and (8) continue to be described by the two-mode truncation even relatively far from the primary bifurcation. Notice, e.g., that for $\Lambda = 2/9$ and $\mu \gtrsim 1.875$ (see Fig. 3a) the uniform states are unstable to at least two nonuniform modes and one might therefore suppose that a two-mode truncation will be of dubious validity. However, we often find that the system (18)–(19) continues to apply (see Fig. 20b and c). This increased range of validity is likely due to the prominence of the heteroclinic bifurcation since for orbits which are approximately heteroclinic the potentially complicated dynamics of the full PDEs are controlled mainly by symmetries and by the local properties of the fixed points O and U where most time is spent; recall that O and U are the same in both the PDEs (7)–(8) and the ODE model (18)–(19). Also important is the fact, mentioned in Section 2, that due to the spatial averaging of the forcing term in Eq. (7) the origin is always stable with respect to nonuniform modes. The higher modes are thus quickly damped under the attracting influence of the trivial state. We conclude that the evident low-dimensional behavior of the PDEs (7)–(8) is related to the presence of the heteroclinic bifurcation involving the origin and its associated cascades. Whenever one is relatively close to these bifurcations in parameter space

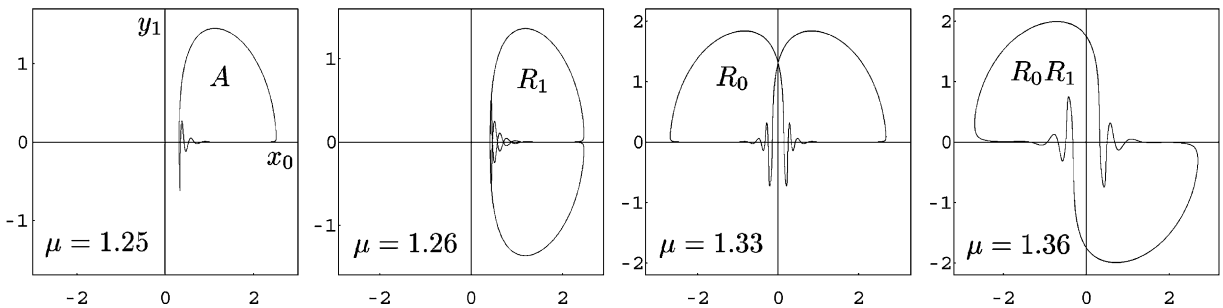


Fig. 19. Stable periodic orbits of the PDEs with different symmetries when $\Lambda = 2/9$. Gluing and symmetry-switching bifurcations, as in the ODEs, appear to be present.

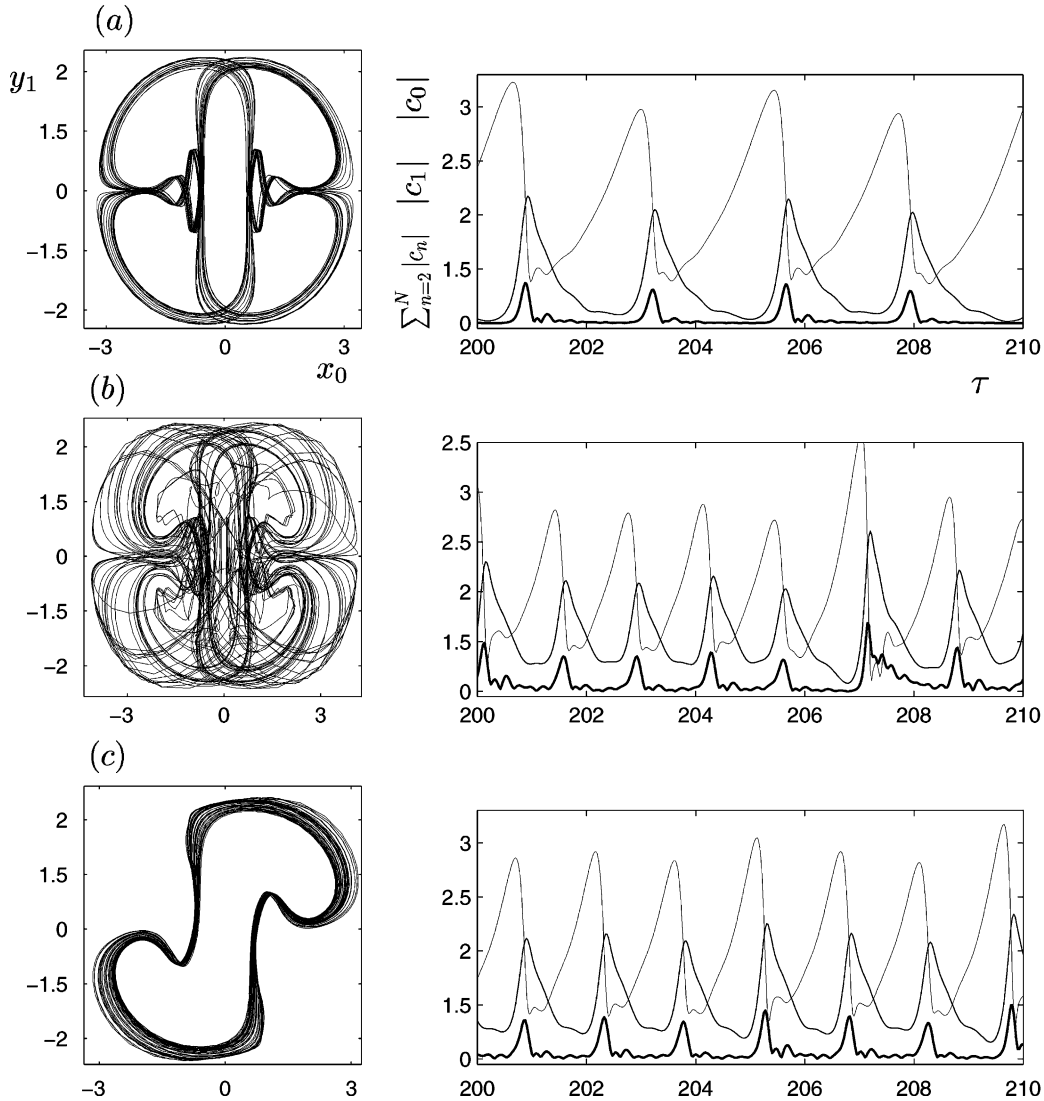


Fig. 20. Relative importance of the Fourier components for $\Lambda = 2/9$: chaotic attractor at (a) $\mu = 1.51$, (b) $\mu = 2.0$, and (c) $\mu = 2.8$. The thin, medium and thick lines correspond to $|c_0|$, $|c_1|$ and $\sum_{n=2}^N |c_n|$, respectively.

(see Fig. 7) the dynamics will typically be dominated by the many periodic and chaotic attractors associated with them (cf. Section 4). For parameter values outside of this regime (e.g. $\mu \gtrsim 3$ when $\Lambda = 2/9$) the dynamics are no longer heteroclinic and hence are more likely to involve other modes. Additional numerical simulations with $\mu \gtrsim 3.5$ (not shown) confirm that the two-mode ODE model no longer gives an adequate description of the PDE dynamics.

When $\Lambda = 2/3$, the value used in [7] for Fig. 1, the heteroclinic bifurcation does not actually occur (see Fig. 7), but the dynamics may nonetheless be dominated by the various periodic orbits and related chaotic attractors which exist in nearby regions of parameter space; gluing bifurcations still occur (see Fig. 18a) even though the full cascade does not. Fig. 21 shows several chaotic attractors for $\Lambda = 2/3$ demonstrating that the dynamics are again dominated

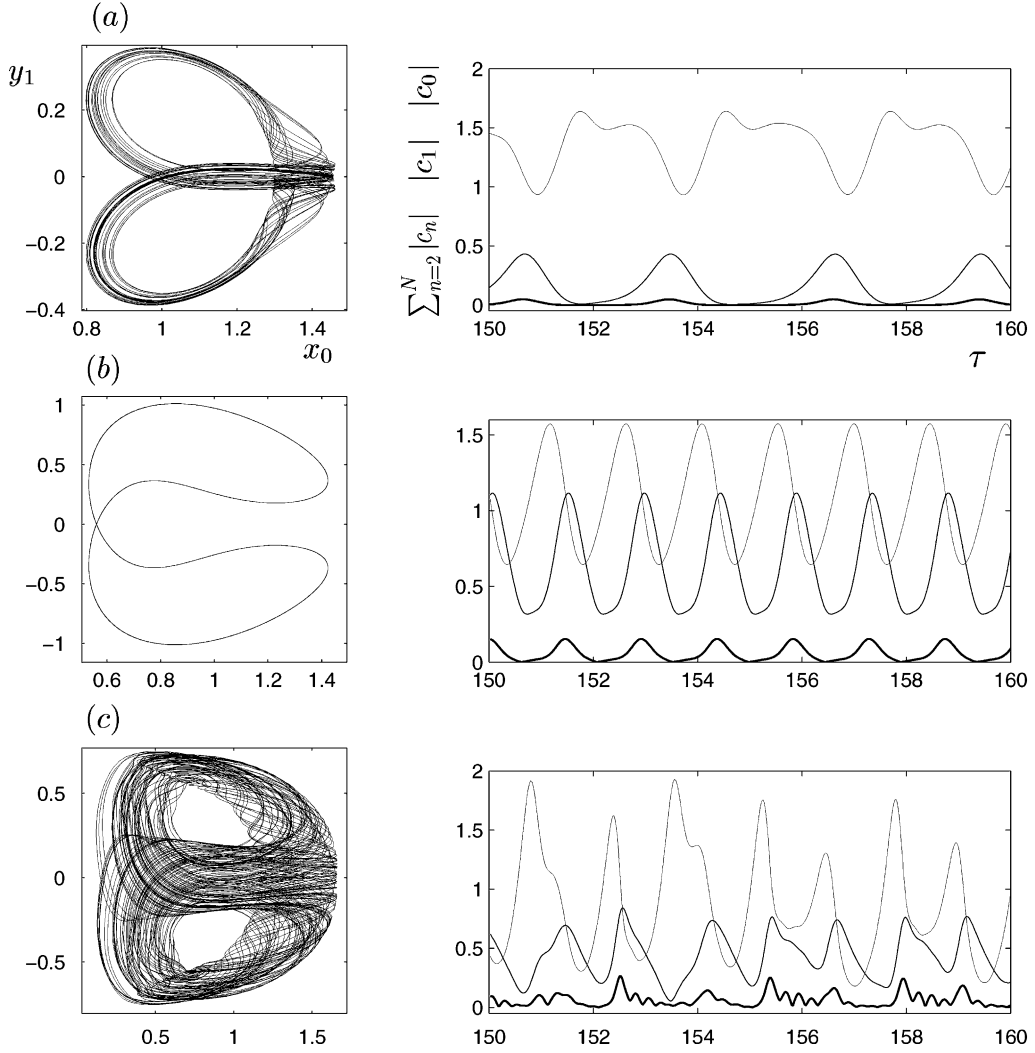


Fig. 21. Relative importance of the different Fourier components when $\Lambda = 2/3$ and (a) $\mu = 1.85$, (b) $\mu = 1.925$, and (c) $\mu = 3.2$. The thin, medium and thick lines correspond to $|c_0|$, $|c_1|$ and $\sum_{n=2}^N |c_n|$, respectively.

by the first two modes. As for $\Lambda = 2/9$, this low-dimensional behavior does not hold for all values of μ and the two-mode ODE model eventually fails. But in contrast to the case $\Lambda = 2/9$, when $\Lambda = 2/3$ this failure can arise for two reasons. The first failure of Eqs. (18) and (19) is due to a \mathcal{R} symmetry-breaking bifurcation, which occurs at $\mu \sim 3.4$. In this case it is not the two-mode nature of the model that becomes inappropriate (the uniform state does not lose stability to the $n = 2$ mode until $\mu \simeq 4.093$) but the restriction to the cosine subspace. Fig. 22a shows a solution, which possesses low-dimensional character but is not reflection-symmetric and is therefore not contained in the system (18)–(19). After a narrow interval ($3.4 \lesssim \mu \lesssim 3.46$) the dynamics recover their reflection-symmetric character, and subsequently (see Fig. 1) a second window of stable uniform states appears for $3.5 \lesssim \mu \lesssim 4.3$. The system becomes abruptly chaotic for $\mu \gtrsim 4.3$, with many modes playing a role in the dynamics and no detectable heteroclinic (or homoclinic) structure. This situation, however, does not persist uniformly as μ is increased even

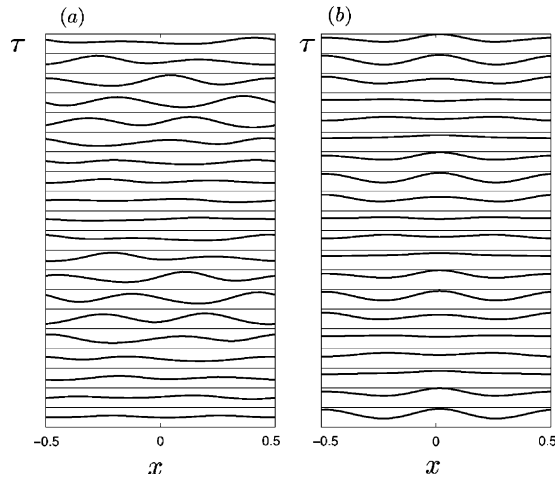


Fig. 22. Space–time diagrams corresponding to (a) a quasiperiodic attractor without reflection symmetry for $\Lambda = 2/3$ and $\mu = 3.4$ and (b) a periodic attractor with reflection symmetry for $\Lambda = 2/9$ and $\mu = 3.46$.

further. In particular, for $\mu = 4.65$ trajectories spend a long time near the invariant *even* subspace ($C_n = 0$ if n is odd), occasionally coming under the influence of unstable periodic orbits in this subspace and being briefly ejected from the even subspace (see Fig. 23). These excursions are associated with episodic drift of the solution (type I drift in the terminology of Martel et al.). This interesting behavior is reminiscent of the so-called blowout bifurcation (see, e.g. [39]) but its description is beyond the scope of the present paper. In the present case, the attractor is completely contained in the even subspace (with dynamics dominated by the first two even modes, $n = 0, 2$, see Fig. 24) over a moderately large interval, $5.0 \lesssim \mu \lesssim 6.5$, but loses stability, apparently in the above manner, as μ decreases below $\mu \simeq 5.0$. We remark that blowout bifurcations provide a general mechanism by which attractors in invariant subspaces lose stability with respect to perturbations out of the subspace.

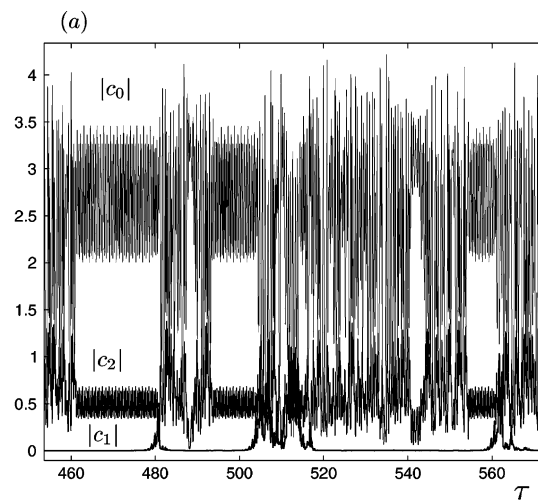


Fig. 23. Norm of the first three modes vs. τ for $\Lambda = 2/3$ and $\mu = 4.65$. The thin, medium, and thick lines denote $|c_0|$, $|c_2|$, and $|c_1|$, respectively. Note the episodic excitation of the mode c_1 .

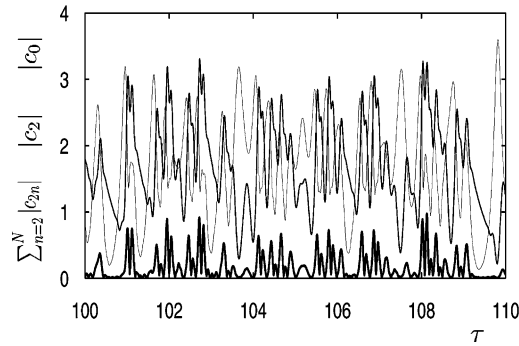


Fig. 24. Relative importance of the even Fourier modes for $\Lambda = 2/3$ and $\mu = 5.5$. The thin, medium and thick lines correspond to $|c_0|$, $|c_2|$ and $\sum_{n=2}^N |c_{2n}|$, respectively.

6. Conclusions

In this paper we have examined in detail the mechanism responsible for the presence of complex dynamics in the damped nonlocal parametrically forced nonlinear Schrödinger equation. Equations of this type arise naturally in the nearly inviscid Faraday system, as well as in optics where they describe pulse propagation down optical fibers with dispersion management. The results shed much light on earlier results for this equation obtained numerically by Martel et al. [7] in the two cases $\Lambda = 2/3, -1$. Positive values of Λ are in general much more interesting. We have seen that for this problem a two-mode Galerkin truncation not only captured the dynamics of the PDEs over a substantial range of forcing amplitudes, but also enabled us to establish that the observed behavior in the PDEs is very likely due to the presence of a heteroclinic connection between nontrivial spatially uniform states and the trivial state. We have seen how the reflection symmetries inherited by the truncation are responsible for the cascades of gluing bifurcations and symmetry-switching bifurcations that accumulate on the heteroclinic bifurcation from opposite sides. We presented the results of an extensive numerical study of the truncated equations demonstrating the presence of these cascades and establishing their scaling properties. Finally, we have used these results to find analogous behavior in the PDEs, thereby extending the study of Martel et al. [7]. The latter paper presents extensive reconstructions of the physically relevant field (1) from the solutions of the PDEs, indicating the various possible types of space–time dependence that results. Identical reconstructions hold for the solutions obtained here. It must be emphasized, however, that these reconstructions ignore the presence of mean flows, and that such mean flows require the solution of a two-dimensional Navier–Stokes equation whenever $|A| \neq |B|$ [11]. This is not, however, an issue for reconstructing the space–time behavior from the solutions $C(x, \tau)$, and the resulting space–time reconstructions resemble Fig. 12c of [7], i.e. patterns of spatially nonuniform standing waves. All such patterns are characterized by a plane of reflection symmetry that is preserved for all time. Since all the coefficients are known (see [6]) a comparison with experiments is in principle possible. Unfortunately, detailed experiments under conditions where Eqs. (2)–(4) or (5) and (6) apply are not yet available. Vega et al. [6] discuss the experimental situation, and suggest appropriate physical parameters for such experiments.

The behavior described in the present paper bears a substantial resemblance to that discussed by Rucklidge and Matthews [27] in their study of the dynamics of the shearing instability in magnetoconvection. This system also has D_2 symmetry and exhibits global bifurcations involving both the origin (corresponding to the conduction state) and the convective state SS. The latter state is reflection-symmetric and can undergo a pitchfork bifurcation to a tilted convection state STC. From a symmetry point of view these states play the same role as O, U and NU in our problem. The essential difference between our system and that studied by Rucklidge and Matthews lies in the fact

that in our case the leading stable eigenvalues of both O and U are complex (the former in the $c_0 = 0$ subspace, and the latter in the $c_1 = 0$). To our knowledge such heteroclinic connections between a pair of saddle-foci have not hitherto been studied (this case was left essentially untreated in [27]), although homoclinic connections to a double saddle-focus have been partially analyzed [40]. Rucklidge and Matthews discuss connections of the form $U \rightarrow O \rightarrow U$ (without encountering the STC states) including the case in which the leading eigenvalues of both O and U are real (cf. [41,42]) and the case in which the least stable eigenvalues of O are complex and in the $c_0 = 0$ subspace while those of U remain real. In the latter case they identify behavior similar to ours, namely cascades of gluing and symmetry-switching bifurcations accumulating on a heteroclinic bifurcation from opposite sides. They point out, moreover, that in contrast to their Galerkin prediction the leading eigenvalues of the U state within their PDEs may in fact be complex. The present paper may therefore be viewed as a detailed investigation of this very interesting case using both general arguments based on appropriate equivariant maps, and specific computational results to illustrate them. In particular the involvement of the NU fixed points (a situation that appears to have little significance for the problem studied in [27]) in the dynamics results in a number of interesting and hitherto unseen complications.

The paper of Rucklidge and Matthews is notable in comparing not only the results from Poincaré maps with those from a system of ODEs but also with PDE simulations. We have followed here the same approach and have likewise been able to demonstrate the utility of both the maps and the drastically truncated Galerkin expansion to the understanding of the dynamics initially observed in the PDEs by Martel et al. [7]. Of course, truncated Galerkin expansions have also been used to study the effect of direct forcing on the sine-Gordon equation, a system much more closely related to ours. Here, too, the study of the finite-dimensional system proved of substantial help in understanding the PDE simulations [21,43]. In the limit of weak forcing and driving the resulting system is a perturbed two-degree-of-freedom completely integrable Hamiltonian system. This Hamiltonian system is identical to the corresponding one in the present system. In particular it possesses a *resonance* consisting of a circle of fixed points each with a pair of symmetry-related homoclinic orbits. The geometric techniques that have been developed to study perturbations of this situation [22–25] provide a detailed picture of the complex multipulse orbits homoclinic to slow periodic orbits or heteroclinic to fixed points, produced by the breakup of the resonance. In the present paper we have explored a different regime, one with a much higher level of both forcing and damping. As a result many (if not most) of the orbits created from the perturbation of the Hamiltonian case are absent. We have seen, however, that there is a great variety of other homoclinic and heteroclinic structures in this regime, made possible fundamentally by the pair of reflection symmetries of Eqs. (20), and that the two-mode model continues to represent these structures faithfully. As emphasized already by Bishop et al. [21,44] this is the reason for the success of the two-mode system as a model of the PDE behavior even at substantial amplitudes. An exploration of the connection between the nearly Hamiltonian dynamics and the ones identified here remains at present unclear, and constitutes an interesting direction for further study.

Acknowledgements

We are grateful to our colleagues C. Martel and J.M. Vega for helpful discussions, and to the NASA Microgravity Program for financial support under Grant no. NAG3-2152.

References

- [1] H. Riecke, J.D. Crawford, E. Knobloch, Time-modulated oscillatory convection, Phys. Rev. Lett. 61 (1988) 1942–1945.
- [2] I. Rehberg, S. Rasenat, J. Fineberg, M. de la Torre Juárez, V. Steinberg, Temporal modulation of traveling waves, Phys. Rev. Lett. 61 (1988) 2449–2452.

- [3] H. Riecke, M. Silber, L. Kramer, Temporal forcing of small-amplitude waves in anisotropic systems, *Phys. Rev. E* 49 (1994) 4100–4113.
- [4] S.G.K. Tennakoon, C.D. Andereck, J.J. Hegseth, H. Riecke, Temporal modulation of traveling waves in the flow between rotating cylinders with broken azimuthal symmetry, *Phys. Rev. E* 54 (1996) 5053–5065.
- [5] J. Miles, D. Henderson, Parametrically forced surface waves, *Ann. Rev. Fluid Mech.* 22 (1990) 143–165.
- [6] J.M. Vega, E. Knobloch, C. Martel, Nearly inviscid Faraday waves in annular containers of moderately large aspect ratio, *Physica D* 154 (2001) 313–336.
- [7] C. Martel, E. Knobloch, J.M. Vega, Dynamics of counterpropagating waves in parametrically forced systems, *Physica D* 137 (2000) 94–123.
- [8] E. Knobloch, J. De Luca, Amplitude equations for travelling wave convection, *Nonlinearity* 3 (1990) 975–980.
- [9] E. Knobloch, J.D. Gibbon, Coupled NLS equations for counter-propagating waves in systems with reflection symmetry, *Phys. Lett. A* 154 (1991) 353–356.
- [10] K. Promislow, J.N. Kutz, Bifurcation and asymptotic stability in the large detuning limit of the optical parametric oscillator, *Nonlinearity* 13 (2000) 675–698.
- [11] E. Martín, C. Martel, J.M. Vega, Drift instability of standing Faraday waves, Preprint, 2001.
- [12] J. Duan, H.V. Ly, E.S. Titi, The effects of nonlocal interactions on the dynamics of the Ginzburg–Landau equation, *Z. Angew. Math. Phys.* 47 (1996) 432–455.
- [13] J.M. Ghidaglia, Finite-dimensional behaviour for weakly damped driven Schrödinger equations, *Ann. Inst. H. Poincaré Anal. Non-linéaire* 5 (1988) 365–405.
- [14] X. Wang, An energy equation for the weakly damped driven nonlinear Schrödinger equations and its application to their attractors, *Physica D* 88 (1995) 167–175.
- [15] O. Goubet, Regularity of attractor for a weakly damped nonlinear Schrödinger equation, *Appl. Anal.* 60 (1996) 99–119.
- [16] M. Oliver, E. Titi, Analyticity of the attractor and the number of determining modes for a weakly damped driven nonlinear Schrödinger equation, *Indiana Univ. Math. J.* 47 (1998) 49–73.
- [17] E. Knobloch, M.R.E. Proctor, N.O. Weiss, Finite-dimensional description of doubly diffusive convection, in: G.R. Sell, C. Foias, R. Temam (Eds.), *Turbulence in Fluid Flows: A Dynamical Systems Approach*, IMA Volumes in Mathematics and its Applications, Vol. 55, Springer, New York, 1993, pp. 59–72.
- [18] L.R. Keefe, Dynamics of perturbed wavetrain solutions to the Ginzburg–Landau equation, *Stud. Appl. Math.* 73 (1985) 91–153.
- [19] J.D. Rodriguez, M. Schell, Global bifurcations into chaos in systems with $SO(2)$ symmetry, *Phys. Lett. A* 146 (1990) 25–31.
- [20] A. Doelman, Finite-dimensional models of the Ginzburg–Landau equation, *Nonlinearity* 4 (1991) 231–250.
- [21] A.R. Bishop, M.G. Forest, D.W. McLaughlin, E.A. Overman II, A modal representation of chaotic attractors for the driven, damped pendulum chain, *Phys. Lett. A* 144 (1990) 17–25.
- [22] G. Kovačič, S. Wiggins, Orbits homoclinic to resonances, with an application to chaos in a model of the forced and damped sine-Gordon equation, *Physica D* 57 (1992) 185–225.
- [23] G. Haller, S. Wiggins, Orbits homoclinic to resonances: the Hamiltonian case, *Physica D* 66 (1993) 298–346.
- [24] G. Haller, S. Wiggins, N -pulse homoclinic orbits in perturbations of resonant Hamiltonian systems, *Arch. Rat. Mech. Anal.* 130 (1995) 25–101.
- [25] G. Haller, S. Wiggins, Multi-pulse jumping orbits and homoclinic trees in a modal truncation of the damped-forced nonlinear Schrödinger equation, *Physica D* 85 (1995) 311–347.
- [26] L.N. Howard, R. Krishnamurti, Large-scale flow in turbulent convection: a mathematical model, *J. Fluid Mech.* 170 (1986) 385–410.
- [27] A.M. Rucklidge, P.C. Matthews, Analysis of the shearing instability in nonlinear convection and magnetoconvection, *Nonlinearity* 9 (1996) 311–351.
- [28] E. Knobloch, Onset of zero Prandtl number convection, *J. Phys. II France* 2 (1992) 995–999.
- [29] M.S. Jolly, I.G. Kevrekidis, E.S. Titi, Approximate inertial manifolds for the Kuramoto–Sivashinsky equation: analysis and computations, *Physica D* 44 (1990) 38–60.
- [30] E.J. Doedel, A.R. Champneys, T.F. Fairgrieve, Y. Kuznetsov, B. Sandstede, X.J. Wang, AUTO 97: Continuation and bifurcation software for ordinary differential equations, 1997, [pub/doedel/auto](http://pub.doedel/auto) at ftp.cs.concordia.ca.
- [31] B. Ermentrout, XPPAUT, Dynamical systems software with continuation and bifurcation capabilities, 2000, [/pub/bardware](http://pub/bardware) at ftp.math.pit.edu.
- [32] E. Knobloch, N.O. Weiss, Bifurcations in a model of double-diffusive convection, *Phys. Lett. A* 85 (1981) 127–130.
- [33] P. Glendinning, C. Sparrow, Local and global behavior near homoclinic orbits, *J. Stat. Phys.* 35 (1984) 645–696.
- [34] S. Wiggins, *Global Bifurcations and Chaos: Analytical Methods*, Springer, New York, 1988.
- [35] J.W. Swift, K. Wiesenfeld, Suppression of period doubling in symmetric systems, *Phys. Rev. Lett.* 52 (1984) 705–708.
- [36] P. Glendinning, Bifurcations near homoclinic orbits with symmetry, *Phys. Lett. A* 103 (1984) 163–166.
- [37] C. Tresser, About some theorems by L.P. Shil'nikov, *Ann. Inst. H. Poincaré Anal. Non-linéaire* 40 (1994) 440–461.
- [38] C.T. Sparrow, *The Lorenz Equations: Bifurcations, Chaos, and Strange Attractors*, Springer, New York, 1982.
- [39] P. Ashwin, J. Buescu, I. Stewart, From attractor to saddle: a tale of transverse instability, *Nonlinearity* 9 (1996) 703–738.
- [40] A.C. Fowler, C.T. Sparrow, Bifocal homoclinic orbits in four dimensions, *Nonlinearity* 4 (1991) 1159–1183.
- [41] A. Arnéodo, P. Coulet, C. Tresser, A possible new mechanism for the onset of turbulence, *Phys. Lett. A* 81 (1981) 197–201.

- [42] D.V. Lyubimov, M.A. Zaks, Two mechanisms of the transition to chaos in finite-dimensional models of convection, *Physica D* 9 (1983) 52–64.
- [43] D.W. McLaughlin, E.A. Overman II, S. Wiggins, C. Xiong, Homoclinic orbits in a four-dimensional model of a perturbed NLS equation: a geometric singular perturbation study, in: *Dynamics Reported*, Vol. 5, Springer, New York, 1996, pp. 190–287.
- [44] A.R. Bishop, R. Flesch, M.G. Forest, D.W. McLaughlin, E.A. Overman II, Correlations between chaos in a perturbed sine-Gordon equation and a truncated model system, *SIAM J. Math. Anal.* 21 (1990) 1511–1536.